



Jomo Kenyatta University of Agriculture and Technology
College of Engineering and Technology
School of Mechanical, Materials, and Manufacturing Engineering
Department of Mechatronic Engineering

Improvement of Wind Tunnel Capabilities for Parachute Testing (FYP 20-2)

Final Year Project Report

**Martin Kinyua (ENM221-0058/2019)
Felix Musanzi (ENM221-0166/2019)**

Supervisors

Dr. Shohei Aoki

Dr. Bernard Owiti

January 2025

Declaration

We hereby declare that the work contained in this report is original; researched and documented by the undersigned students. It has not been used or presented elsewhere in any form for award of any academic qualification or otherwise. Any material obtained from other parties have been duly acknowledged. We have ensured that no violation of copyright or intellectual property rights have been committed.

1. Martin Kinyua

Signature..... Date.....

2. Felix Musanzi

Signature..... Date.....

Approved by supervisors:

1. Dr. Shohei Aoki

Signature..... Date.....

2. Dr. Bernard Owiti

Signature..... Date.....

Acknowledgment

We wish to express our sincere appreciation for the invaluable assistance provided during the development of this project. First and foremost, we thank the Lord Almighty for His grace and provision throughout this journey.

We extend our gratitude to our project supervisors, Dr. Shohei Aoki and Dr. Bernard Owiti, for their wise counsel and unwavering guidance. Special thanks to our project coordinator, Dr. Antony Muchiri, and members of the Fluid Dynamics Research Group, Dr. Meshack Hawi and Dr. Patrick Muiruri, for their continued assistance and expertise.

We also acknowledge the contributions of Mr. K. Chau, our technologist, Mr. Mwandi, our fluids lab technician, and all other workshop technicians for their guidance and practical advice. We are deeply grateful for their encouragement and look forward to continuing to learn from them.

Abstract

Parachutes are critical for rocket recovery, but existing testing methods, such as drop tests, lack precision and repeatability. JKUAT's wind tunnel, while useful for general testing, is not equipped to handle parachute-specific experiments.

This project focuses on upgrading the wind tunnel to facilitate accurate and controlled parachute testing. The enhancements include implementing a active grid system to transition airflow between laminar and turbulent states, developing a modular test rig for mounting and testing parachutes with minimal interference, and designing a dual parachute system for a 20 kg rocket.

The upgraded wind tunnel allows detailed measurements of drag force and turbulence effects, providing essential data to refine parachute designs. These improvements aim to ensure safer and more reliable rocket recovery through precise and repeatable testing.

Contents

Declaration	I
Acknowledgment	II
Abstract	III
1 Introduction	1
1.1 Background	1
1.2 Problem statement	3
1.3 Objectives	4
1.4 Justification of the Study	5
1.5 Scope	5
2 Literature Review	6
2.1 Introduction	6
2.2 Description of existing tests	6
2.2.1 Wind tunnel tests	6
2.2.2 Drop Tests	7
2.2.3 Flight Tests	8
2.3 A focus on wind tunnel testing	10
2.3.1 Turbulence generation	10
2.3.2 Characteristics of turbulence	14
2.4 Development of dual recovery sytsem	15
2.4.1 Key Features of Parachute Development	16
2.5 Test rig structure	17
2.5.1 Integration to wind tunnel	17
2.5.2 Instrumentation and data collection	19
2.6 Gap analysis	20

3 Methodology	22
3.1 Mechanical module	22
3.1.1 Active grid subsystem design	22
3.1.2 Active grid subsystem material consideration	23
3.1.3 Fabrication and assembly of the active grid system	29
3.1.4 Active grid system subassembly	32
3.1.5 Design considerations of the test rig	33
3.1.6 Design of the test rig structure	33
3.1.7 Fabrication of test rig	36
3.1.8 Parachute design	37
3.1.9 Model parachute design	48
3.1.10 Parachute fabrication	49
3.2 Electrical circuit design	51
3.2.1 Motor selection and sizing	51
3.2.2 Stepper Motor consideration	52
3.2.3 Stepper motor driver	53
3.2.4 Limit switches	53
3.2.5 Sensors	54
3.2.6 Power Budget	55
3.2.7 Electrical circuit fabrication	57
3.2.8 Instrumentation setup	58
3.3 Control module design	59
3.3.1 Micro-controller selection	60
3.3.2 Software Implementation	60
3.4 CFD Simulation	61
3.4.1 Simulation Setup	62
3.4.2 Geometry and Mesh	62
3.4.3 Boundary Conditions	63
3.4.4 Validation of CFD model	63

3.4.5 Post-Processing and Analysis	64
4 Results and Discussion	65
4.1 Mechanical Module	65
4.2 Electrical and Control Systems	68
4.2.1 Instrumentation System	70
4.3 CFD Results	71
4.3.1 Velocity distribution on model parachute	71
4.3.2 Dynamic pressure distribution	72
4.4 Testing	73
4.5 Parachute implementation	75
5 Conclusion	77
References	79
6 Appendix	83
A Time Plan	83
B Budget	84
C Drawings	85
C.1 Active grid system design drawing	85
C.2 Parachute holder drawing	86
C.3 Test rig design drawing	87
C.4 Frame design drawing	88
C.5 Flap shaft design drawing	89
C.6 Flap design drawing	90
C.7 Limit switch subassembly design drawing	91
C.8 Top perspex design drawing	92
C.9 Bottom perspex design drawing	93

C.10 Sides perspex design drawing	94
C.11 Circuit board housing design drawing	95

List of Figures

2.1	NASA's Ames Wind tunnel	7
2.2	Drop test from a known height	8
2.3	Boeing Starliner flight tests(left), SpaceX Crew dragon flight test(right) . .	9
2.4	Passive grid located at the entrance of a test section	11
2.5	Roughness elements just before test section in a wind tunnel	11
2.6	Active turbulence Generator	13
2.7	Dual recovery system	15
2.8	Test Rig Structure	18
2.9	Schematic of the test setup used in the Lockheed-Ga. wind tunnel.	19
3.1	Shapes and their drag coefficients	23
3.2	Flap design	27
3.3	Motor holder design	28
3.4	Bearing to flap shaft to coupler subassembly	30
3.5	Flap and shaft subassembly	31
3.6	Flap shaft	31
3.7	Top frame for attaching stepper support	32
3.8	Stepper motors attached to stepper holder	32
3.9	Test rig design	36
3.10	Test rig	37
3.11	Main Parachute Canopy design-Top View	43
3.12	Fabricated model parachute	50
3.13	Limit switch	54
3.14	Electrical circuit design	56
3.15	Fabricated electrical circuit	58
3.16	Sensors used	59
3.17	Interface modules	59
3.18	Instrumentation setup	59

3.19	Mesh generated for CFD simulation of the parachute geometry	62
3.20	Simulated drag force of the full scale parachute	63
4.1	2D drawing of AGS and test section	66
4.2	3D model of AGS and test rig	67
4.3	Fabricated AGS and test section	68
4.4	Wiring diagram of the circuit	69
4.5	Fabricated electronic circuit	70
4.6	Instrumentation setup	71
4.7	Velocity contour plot	72
4.8	Dynamic pressure contour plot	73
4.9	Parachute expansion	73
4.10	Preliminary test showing drag coefficient values at approximately 15m/s .	74
4.11	Fabricated parachutes	76
C.1	Active grid system design drawing	85
C.2	Parachute holder design drawing	86
C.3	Test rig design drawing	87
C.4	Frame design drawing	88
C.5	Flap shaft design drawing	89
C.6	Flap design drawing	90
C.7	Limit switch drawing	91
C.8	Top perspex design drawing	92
C.9	Bottom perspex design drawing	93
C.10	Side perspex design drawing	94
C.11	Bottom perspex design drawing	95

List of Tables

3.1	Material Comparison for flap material selection	25
3.2	Perspex Material Width at Full Force (52.3N)	26
3.3	Minimum Rod Diameters for Small Deflection	35
3.4	Drogue parachute summary table	41
3.5	Main parachute summary table	44
3.6	Parameters and Opening Shock Forces for Main and Drogue Parachutes . .	46
3.7	Shock Cord Dimensions and Strength	47
3.8	Power requirements for the components in the active grid system.	55
4.1	Fabrication Details of Main and Drogue Parachutes	75
A.1	Budget	83
B.1	Budget	84

1 Introduction

1.1 Background

Nakuja, a university-based amateur rocketry group at JKUAT, plans to participate in the 2025 Spaceport America Cup—the world’s largest intercollegiate rocket engineering competition [1]. Successful participation requires adherence to the International Rocket Engineering Competition (IREC) guidelines. According to these guidelines, any launch vehicle anticipated to reach an apogee above 457 m (1,500 ft) above ground level (AGL) must employ a dual-event recovery system, defined as follows:

- Drogue Deployment Event: A drogue parachute (or reefed main parachute) must deploy at or near apogee.
- Main Deployment Event: A main parachute must deploy at a much lower altitude, or the reefed main parachute must unreef.

This requirement underscores the urgency for Nakuja to develop a dual-event recovery system [2].

This project aims to design and test a parachute system that strictly adheres to the IREC guidelines. To achieve this, Nakuja aims to advance from traditional drop tests to wind tunnel testing.

Wind tunnels are essential tools in aerospace engineering, providing controlled environments to test the aerodynamic properties of objects such as aircraft, rockets, and parachutes [3]. These facilities allow engineers to simulate various flight conditions and gather critical data to inform design and improve performance. Traditional wind tunnels typically provide either laminar or turbulent flow, but advanced testing scenarios often require the ability to transition between these flow states.

Transitioning between flow states can give vital data by simulating real-world atmospheric

conditions during parachute flight. When a parachute is deployed, it experiences a range of flow conditions, from the initial laminar flow as it opens to potentially turbulent flow as it stabilizes and descends. This detailed information helps engineers to refine parachute designs, ensuring they can withstand the diverse conditions they will encounter in actual use. By accurately simulating these conditions, we can develop parachutes that are more reliable and effective, enhancing the safety and success of missions involving spacecraft and other aerospace vehicles.

However, existing wind tunnel infrastructure often lacks the ability to automatically vary flow conditions and measure turbulence. Furthermore, the absence of a modular test rig limits the scope of testing for different parachute configurations.

1.2 Problem statement

The ideal scenario for research and development of a parachute would involve having convenient access to wind tunnel with varying flow states. Transitioning between flow states is necessary for accurately recreating the turbulent environments encountered by parachutes during descent.

Currently, parachute testing in NAKUJA relies on drop tests, which lack the precision and repeatability of controlled wind tunnel experiments [4]. Drop tests also typically yield fewer data points due to the nature of free-fall dynamics compared to the continuous measurements possible in wind tunnels [5].

By upgrading the wind tunnel to include the AGS and generate turbulence, this project seeks to transition from drop testing to wind tunnel testing. This approach not only enhances the accuracy of the tests but also allows for detailed investigation of aerodynamic forces and deployment dynamics under varied flow conditions.

1.3 Objectives

Main Objective

The main objective is to upgrade the existing wind tunnel to provide flow conditioned environment while developing the parachutes for N-4 rocket for testing and analysis.

Specific Objective

1. To design and fabricate an active grid system structure, a test rig and a robust parachute system for testing in the wind tunnel.
2. To design and develop an electrical circuit for actuation of the active grid system.
3. To implement control algorithms for flow conditioning.
4. To analyze sensor data to extract meaningful information.

1.4 Justification of the Study

Upgrading the wind tunnel with an Active Grid System addresses the need for parachute testing in a controlled environment. Current methods, such as drop tests, lack the precision and repeatability needed to thoroughly understand parachute behavior under various conditions.

This project enables Nakuja's researchers to conduct in-depth tests and analyses of parachute performance, allowing a more data driven design process for parachute fabricataion.

1.5 Scope

The project involves developing an active grid system (AGS) and testing a model parachute within the wind tunnel to evaluate its aerodynamic performance and deployment behavior.

2 Literature Review

2.1 Introduction

Testing of a parachute system is critical for ensuring the system has the required reliability. Preferably the system should be tested in conditions as close to the actual flight conditions as possible. This, is however, not always in the technical or budgetary capabilities of a project. To still be able to test the system, one can test a parachute system in various ways ranging from frequently used to more experimental.

2.2 Description of existing tests

2.2.1 Wind tunnel tests

The standard way of testing a parachute in a controlled environment is by using a wind tunnel. In a wind tunnel, the test object (parachute) is stationary and the air (wind) is moved around the test object. Wind tunnels range from the very large, such as NASA's Ames Wind tunnel, illustrated in figure 2.1, with a 24m x 36m test sections to tiny wind tunnels with a test section of 10cm x 10cm. The testing speeds can vary significantly from hypersonic speeds ($>$ Mach5) to no more than 30m/s [6]. Wind tunnels can assist in identifying the drag capabilities and stability parameters of a parachute and serve as a verification tool for computational fluid dynamics

(CFD) results. The CFD can then be used to expand the knowledge of the parachute's behaviour.

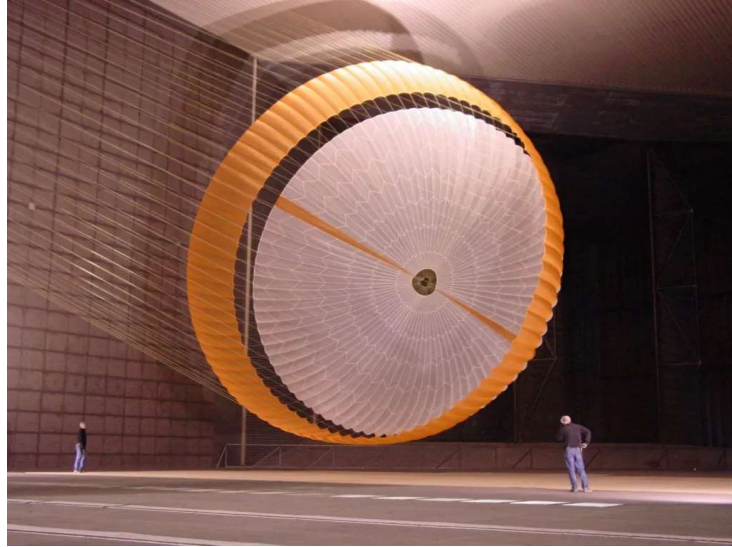


Figure 2.1: NASA's Ames Wind tunnel

[6]

2.2.2 Drop Tests

Another type of test is the drop test as illustrated in figure 2.2. In this test, one attaches the parachute system to a payload and drops it from a known height. Dependent on the body the parachute system is attached to, the speeds which can be achieved are still significantly high, even supersonic speeds [7]. Drop tests can be performed at various heights ranging from large cranes to helicopters and aeroplanes to high altitude balloons. Examples of this can be seen in the Boeing Starliner drop tests, which used a Starliner parachute system attached to a dart-shaped sled the same weight as a Starliner. This was performed to confirm the functioning of a



Figure 2.2: Drop test from a known height

redesigned and strengthened soft link joint that is part of the network of lines connecting the parachutes to the spacecraft. The test also validated a change to strengthen one textile joint in the parachute, increasing overall parachute robustness [8].

2.2.3 Flight Tests

When both the drop test and the wind tunnel test do not give the desired conditions, one can resort to flight testing. During these often costly tests, a system is exposed to the actual flight conditions. A parachute system is tested on a sub-orbital rocket or put on the first stage on an orbital rocket. Here both supersonic re-entry conditions can be achieved. This testing method was used for Vorticity's SuperMax experiment proving the supersonic deployment behaviour of a disk gap band parachute [9]. As well as ESA's ARD experiment to test an entire re-entry capsule, including the

parachute system [10]. Both these missions were suborbital. A near orbital mission was the OREX mission performed by JAXA [11].

Final examples of flight testing are the SpaceX Demo-1 (uncrewed first flight of the Crew dragon) [12], SpaceX Demo-2 (first crewed flight of the Crew dragon) [13], and the Boeing Starliner missions shown on figure 2.3. All the missions reviewed above included parachute testing as a critical component of its objectives. The parachute system was rigorously tested during these missions. This included the deployment of main parachutes and drogue parachutes to ensure safe re-entry and landing. The performance of these parachutes was closely monitored.

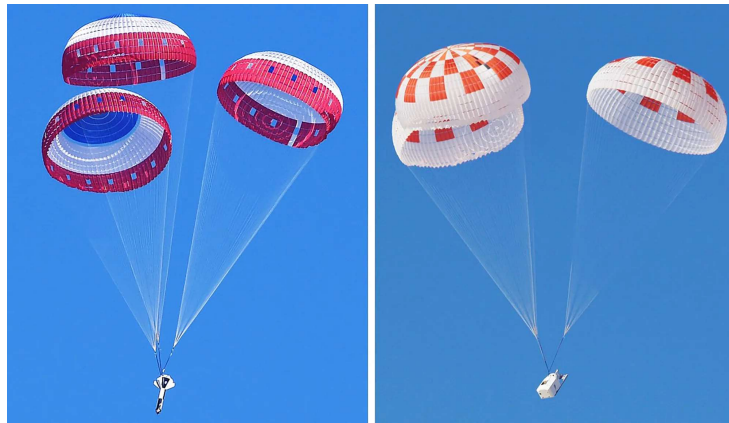


Figure 2.3: Boeing Starliner flight tests(left), SpaceX Crew dragon flight test(right)

These tests are the most representative test for the Entry, Descent, and Landing system and are favoured to verify multiple requirements in one test. They also give a very comprehensive data set for future missions and tests. However, organising and performing these tests take up a significant amount of resources. Furthermore, when one of these tests fails, it will be

challenging to determine the root cause.

2.3 A focus on wind tunnel testing

JKUAT is fortunate to have a subsonic wind tunnel that can provide a laminar flow [3]. While laminar flow is often desired, turbulent flow is sometimes needed to study the effects of turbulence on test subjects. Therefore, various methods and considerations for generating controlled turbulence in wind tunnels have been examined.

2.3.1 Turbulence generation

1. Use of passive grids

One widely used method to generate turbulence in wind tunnels is the use of grids and screens within the test section. These devices create turbulence through their interaction with the flow, producing vortices and fluctuations in velocity that mimic natural turbulent flows [14]. The design and spacing of grid elements are critical in determining the characteristics of the generated turbulence. However, these grids are static as illustrated in figure 2.4, and do not allow for adjustment, limiting the ability to vary turbulence intensities and scales.

2. Use of roughness elements

Another effective method for generating turbulence in wind tunnels is the use of roughness elements placed on the walls as illustrated in

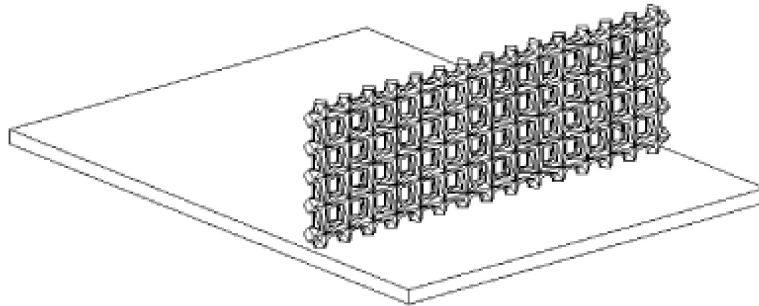


Figure 2.4: Passive grid located at the entrance of a test section

[15]

figure 2.5. These elements perturb the boundary layer and generate turbulence through frictional interactions with the flow [16]. Numerous experiments have been conducted to study flow characteristics over a variety of large-sized roughness elements. However, in most cases, the geometry of the wall roughness was chosen by trial and error rather than based on its ability to produce predictable wall shear stress or velocity distributions [17].

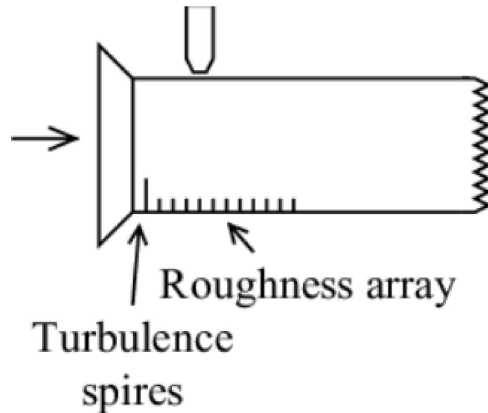


Figure 2.5: Roughness elements just before test section in a wind tunnel

One significant limitation of this method is the unpredictability in the

resulting turbulence characteristics. The choice of roughness geometry can significantly influence the flow field, and without a systematic approach, achieving the desired turbulence properties can be challenging. Therefore, while roughness elements are useful, there is a need for more controlled and predictable methods to generate turbulence in wind tunnels [17].

3. Active Turbulence generator

The simplest and most effective way to create a turbulent flow field is through the use of a turbulence grid. However, with this static method, the turbulence intensity and vortex scale generated are often limited, meaning the overall effects of the turbulence are constrained [18].

To address these limitations in a grid-generated turbulent field, one might consider increasing the flow velocity or enlarging the grid size. However, these approaches are often restricted by the capabilities of the available equipment. As a result, various dynamic turbulence generation devices have been developed and evaluated to overcome these challenges [18].

Makita et al. [19] devised a dynamic turbulence generating mechanism in which 15 rotating shafts with many mixing blades attached to each of the 15 vertical and horizontal axes are independently vibrated randomly invertedly by a pulse motor to disturb the airflow. As a result, they succeeded in creating a large-scale, high-quality quasi-isotropic

turbulent field with a clear inertial subregion in a small wind tunnel with a cross-section of 700mm^2 shown in figure 2.6.

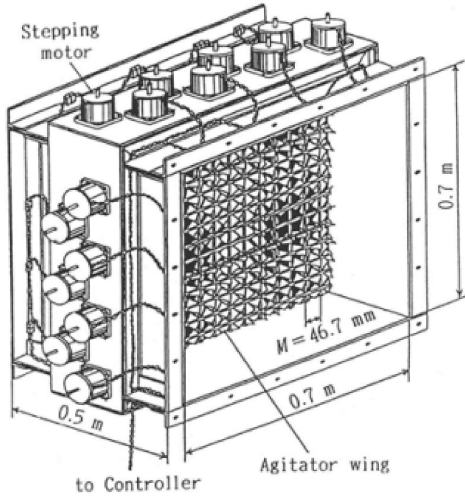


Figure 2.6: Active turbulence Generator

[18]

This method can easily create a turbulent field with a large Re number in a small wind tunnel, and is used in various research institutes both in Japan and abroad, and its usefulness has been widely recognized. However, the current turbulence generator, which operates with a simple digital circuit control system, is limited to basic random inversion vibrations[18].

This limitation hinders the ability to adjust the amplitude of the stirring blades and control vortex scale and turbulence intensity, which are crucial for studying turbulent phenomena. Moreover, the existing system lacks the capability to generate large-scale velocity shear flows typically found in the atmospheric surface boundary layer [18, 19].

2.3.2 Characteristics of turbulence

Reynolds number is a dimensionless quantity measuring the ratio between inertial and viscous forces to predict fluid flow patterns. It is used to predict the transition from laminar to turbulent flow and for scaling in fluid dynamics.

The Reynolds number (Re) is given by the formula:

$$Re = \frac{\rho v L}{\mu} \quad (2.1)$$

where:

- ρ is the fluid density in kilograms per cubic meter (Kg/m^3),
- v is the flow velocity in meters per second (m/s),
- L is a characteristic linear dimension such as diameter measured in meters (m),
- μ is the dynamic viscosity of the fluid in Pascal-seconds ($Pa \cdot S$)

At low Reynolds numbers ($Re < 2,300$), the flow is typically laminar, meaning the fluid layers move in smooth, parallel paths. Viscous forces dominate, and the flow is stable.

As the Reynolds number increases ($2,300 < Re < 4,000$), the flow enters a transitional regime where it can fluctuate between laminar and turbulent flow. This is the critical Reynolds number range where turbulence can

start to develop.

At high Reynolds numbers ($Re > 4,000$), the flow becomes fully turbulent. Turbulent flow is characterized by rapid mixing and energy dissipation. The high value of the Reynolds number predicts the turbulent nature of the flow, while a low value indicates laminar flow.

2.4 Development of dual recovery system

These systems use two stages of parachute deployment: a small drogue parachute and a larger main parachute. The drogue parachute is deployed at apogee, stabilizing the rocket's descent without significantly slowing it down. This allows the rocket to descend quickly and minimize drift. At a predetermined lower altitude, the main parachute is deployed, slowing the descent for a safe landing [20].

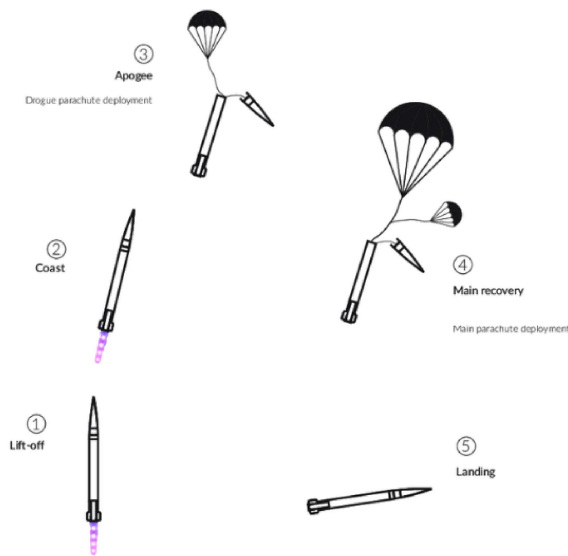


Figure 2.7: Dual recovery system

Advantages of Dual Recovery Systems:

Dual recovery systems offer several advantages for rocket recovery. By deploying the main parachute at a lower altitude, they effectively reduce horizontal drift, ensuring that the rocket remains closer to the launch site. Additionally, the drogue parachute stabilizes the descent, reducing the risk of tumbling and potential damage. Third, the two-stage deployment ensures a more controlled and safer descent, which is especially important during high-altitude flights.

Modern dual recovery systems often incorporate electronic components such as altimeters and accelerometers to precisely control the deployment of the parachutes. These electronics ensure accurate deployment at the right altitudes, enhancing the reliability and safety of the recovery process [20, 21].

2.4.1 Key Features of Parachute Development

Parachute selection frequently begins with the stability requirement. This requirement limits the oscillation of the parachute, so that a high level of stability automatically eliminates many types of high-drag parachutes or involves the use of parachute clusters.

Weight and volume are also very important considerations, which strongly influence the landing. Normally the structure of a parachute system constitutes 5% of the total weight of a light vehicle, or 3-4% for heavier vehicles. According to Lenov et al. [22] the main requirements to the parachute

means of delivery, depending on the characteristics of the object being dropped are: ensuring the object safety, range of application conditions, its flight altitude and velocity, the altitude above sea level of the landing site, the atmosphere parameters and the wind velocity near the landing site.

Reliability, maintenance and re-usability are factors that directly influence the cost and success of the parachute system. High reliability reduces the risk and associated costs of failures. Regular maintenance ensures continued safe operation. Re-usability can offer long-term cost savings despite higher initial investment and refurbishment needs [23, 24].

2.5 Test rig structure

2.5.1 Integration to wind tunnel

According to Berger [25], the test rig structure, illustrated on figure 4.6 must be constructed from materials capable of withstanding the forces exerted by the parachute and the airflow. Common materials include aluminum and steel, which offer a balance of strength and weight. The rig must also be designed to minimize aerodynamic interference with the parachute and airflow [26].

Michael Macha- a senior member of technical staff, parachute systems division, AIAA- notes, after his own testing and research, that it is good practice to make the test rig(strut) as small and as streamlined as possible

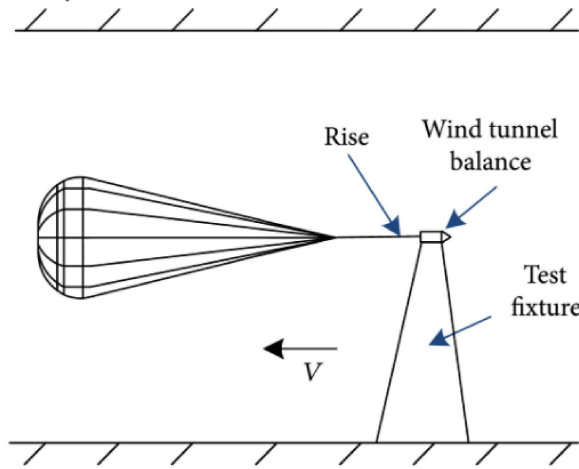


Figure 2.8: Test Rig Structure

[27]

when only the parachute parameters are required [28]. He further notes that the effect may be small if the strut has a streamlined cross section, but should still be estimated in terms of the reduction in dynamic pressure over the frontal area of the inflated canopy.

Further in his paper [28] he notes that whenever a single, floor-mounted, streamlined strut is used, care should be taken that the strut is at zero angle of incidence with respect to the tunnel flow. Otherwise, even a slight angle of attack may produce a vortex on the centerline of the tunnel of sufficient strength to cause the parachute to rotate.

For these limitations Macha proposes a convenient and economical alternative to a strut support. He proposes to instead hold the parachute in place with three or more wires or thin cables anchored in the tunnel walls [28]. With a cable system, an internal balance (described in the next section) is required to measure the aerodynamic forces on the parachute.

Additionally, the design should incorporate features that allow for easy adjustment and reconfiguration. This flexibility can accommodate different parachute sizes and types, as well as varying test conditions.

2.5.2 Instrumentation and data collection

Much of parachute testing in wind tunnels involves time-averaged data for a model of fixed configuration under steady airflow conditions. The usual measurement for this kind of test is parachute drag, or in the case of nonsymmetric canopies, drag plus a normal force (i.e., lift). To determine the forces, two types of balances are in general use: external balances which carry the model loads outside the test section before they are measured, and internal balances, which fit into the forebody and send data out through electrical wires. Either type may be used if the forebody is strut supported. An internal balance is required if the forebody is supported by cables [28].

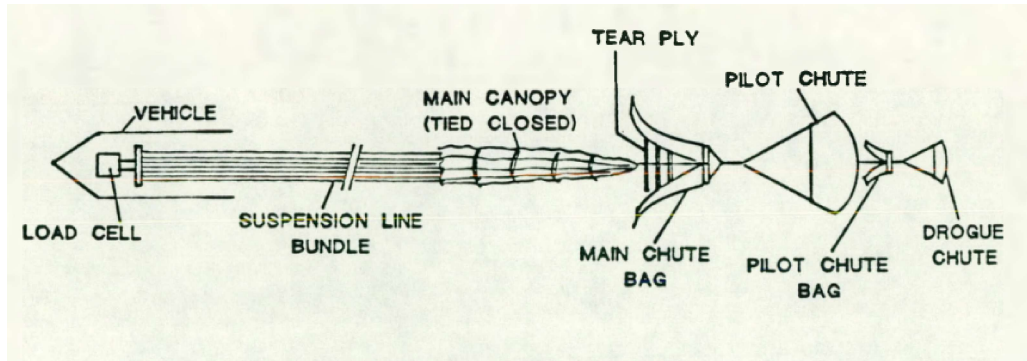


Figure 2.9: Schematic of the test setup used in the Lockheed-Ga. wind tunnel.

Sensors such as load cells, pressure transducers, and high-speed cameras are commonly used [28]. Figure 2.9 systematically shows the components of

a system that was tested in a wind tunnel. The placement and calibration of these instruments are critical for obtaining precise data. Advances in data acquisition systems have enhanced the ability to capture detailed measurements in real time.

The load cells measure the forces exerted on the parachute and rig, providing data on the drag and lift forces. Pressure transducers are used to measure the pressure distribution over the parachute canopy, which is crucial for understanding aerodynamic performance. High-speed cameras may capture the deployment sequence, allowing a detailed analysis of the dynamic behavior of the parachute [28].

Other measurements that are sometimes made include canopy surface pressure and canopy fabric stress.

2.6 Gap analysis

Through careful analysis, it becomes evident that the existing solutions for parachute testing suffer from several limitations. Both drop tests and flight tests face challenges in controlling environmental variables, which can lead to inconsistent results. Flight tests are expensive and resource-intensive, making them less feasible for frequent evaluations. While drop tests and flight tests provide valuable data, they may not capture all necessary parameters for comprehensive analysis due to the complexities involved in real-world scenarios. Wind tunnel testing on the other hand offers a con-

trolled, cost-effective alternative that enhances data collection capabilities and allows for iterative design improvements. By integrating wind tunnel testing into the development process, a more robust evaluation of parachute systems can be achieved, ultimately leading to safer and more reliable performance in operational scenarios.

3 Methodology

This section shows the design process used in implementing this project. The main purpose of this system was to vary the airflow within the wind tunnel from laminar to turbulent flow. The system consists of three main parts: the mechanical, electrical, and control modules.

3.1 Mechanical module

The mechanical module consists of the following subsystems:

- An Active Grid System Contains flaps that rotate to disturb the airflow in the wind tunnel, transitioning it from laminar to turbulent.
- A test rig structure: The structure that holds the model parachute within the test section, ensuring stability and proper positioning during wind tunnel experiments.
- Parachutes: Drogue, Main, and model parachute.

3.1.1 Active grid subsystem design

The active grid system (AGS) is a motorized turbulence generation device. It is designed to be installed at the entrance to the wind tunnel test section and consists of five vertically aligned flaps controlled by individual stepper motors to manipulate airflow dynamically.

3.1.2 Active grid subsystem material consideration

The grid subsystem consists of flaps, stepper housing and test section

1. Flaps

The flaps key considerations are material selection, laminar flow interference, tensile strength of the material, and blockage area:

(a) Flow interference level

The shapes of the flaps are key since they induce different drag forces incorporation disturbance during the lamina flow. Figure 3.1 shows different shapes with their drag coefficients.

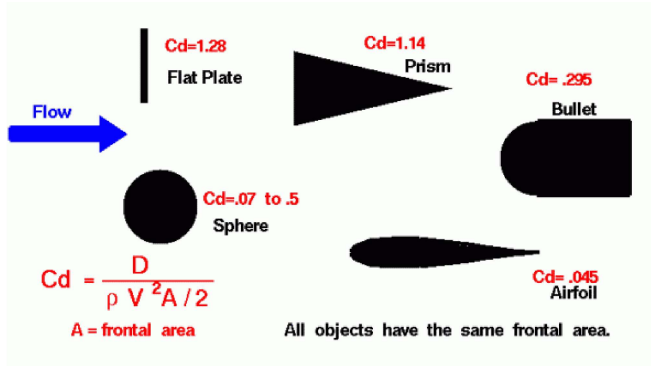


Figure 3.1: Shapes and their drag coefficients

[29]

The airfoil, flat rectangular sheet, and cylindrical rods with flat rhombus flaps are considered since they have a minimal drag coefficient.

(b) Blockage area effect to flow

This is the area covered by the obstacle (flaps) to the flow in the

test section resulting in flow velocity reduction. Comparing the considered shapes, a flat rectangular sheet has a minimal blockage area when both are placed parallel to the flow.

(c) Material considerations

The material must be sufficiently strong to withstand the forces induced by airflow. This ensures that it can resist bending during flow disturbances. To prevent deflection and maintain structural integrity, the thickness of the sheet should be calculated based on the material's properties and the expected load.

The force exerted on the sheet is determined by the pressure difference across its surface. Given that the sheet is oriented perpendicular to the airflow, we can calculate the force using the following relationship:

$$F = P \times A \quad (3.1)$$

Where:

- F is the force exerted on the sheet.
- P is the total pressure difference, which is primarily the dynamic pressure since there is no significant static pressure difference.
- A is the area of the sheet facing the airflow, which is 0.1936 m^2 .

The dynamic pressure can be calculated using the formula:

$$q = \frac{1}{2} \rho v^2 \quad (3.2)$$

Where:

- q is the dynamic pressure.
- ρ is the fluid density, approximately 1.225 kg/m^3 .
- v is the fluid velocity, given as 21 m/s .

Based on these calculations, the force exerted on the sheet is approximately 52.3 N .

Arriving at the optimum width of a sheet, the maximum force was developed towards a single sheet, then the maximum force, and the optimum width with minimum thickness was acquired thus allowing use of 5 sheets for the force distribution. The material comparison of the sheets is as shown in table 3.1 below

Table 3.1: Material Comparison for flap material selection

Material	Advantages	Disadvantages
Perspex	Lightweight, cost-effective, low turbulence.	Less durable, not as strong as metals.
Aluminum	Lightweight, strong, corrosion-resistant.	Requires wider flaps for strength, more expensive.
Mild Steel	Strong, durable, cost-effective for high-strength needs.	Heavier, increases motor torque, more expensive and harder to work with.
Stainless Steel	Very strong, durable, corrosion-resistant.	Heavier, increased motor torque, expensive.
ABS Plastic	Lightweight, cost-effective, easy to work with.	Requires wide flaps for strength, not suitable for high-strength needs.

Perspex is chosen for its lightweight nature, cost-effectiveness and

its availability in the workshop. Additionally, Perspex is easier to work with compared to metals like aluminum or steel, while still offering sufficient durability for the system's requirements. Its thickness and width necessary to provide structural integrity was calculated and variations as shown: Determining the appropriate width of the sheets for different materials considered at different thickness sizes:

- Force applied, $F = 52.3\text{N}$
- Length of the beam, $L = 0.44\text{ m}$
- Thickness of the sheet, $t = (2\text{ mm}, 3\text{ mm}, \text{ or } 4\text{ mm})$.
- . Perspex, $\sigma_{yield} \approx 70\text{ MPa}$

For a simply supported beam with a point load P at the center, the minimum width is given by the formula shown.

$$b = \frac{PL^3}{4E\delta_{max}t^3}$$

The results comparison for the thicknesses are as shown in the table 3.2 below

Table 3.2: Perspex Material Width at Full Force (52.3N)

T (mm)	Width at Full Force (52.3N)
2	530.57 mm
3	159.40 mm
4	66.32 mm

A range of width of 50mm to 100mm is suitable practically due

to wind tunnel dimension limitation, cost, weight, and blockage area restriction to minimize turbulence during lamina flow.

Too wide a flap will result in increased weight of flap that will increase torque requirement for motor thus more powerful, expensive stepper motors. The dimensions will also fail to fit the wind tunnel test section size. Too narrow flaps will result in more flaps occupying the section thus increasing the number of motors to be used. This will also result in a higher blockage area.

Therefore 4mm thickness, 85mm width perspex was chosen to be optimal to obtain a total of 5 flaps from the equation below.

$$No.of\ flaps = \frac{Width_{AGS}}{Width_{Flap}} \quad (3.3)$$

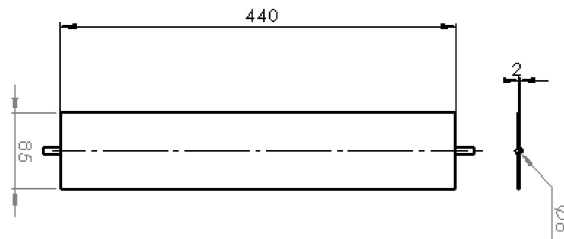


Figure 3.2: Flap design

Bearings and couplers

Couplers are used for firm interconnection between the flap rods and stepper motor shafts. Flexible couplers are more appropriate than rigid and flange couplers since they account for misalignments and vibrations while maintaining high precision. A Flexible coupler of 8mm to 8mm diameter is selected.

Bearings are used for connection between the coupler and the frame to ensure a smooth rotation of the flaps within the AGS. Ball bearings offer the work sufficiently. A sealed ball bearing with an internal diameter of 13 mm is selected to ensure no air leakage to the outside environment. This choice is made because the selected coupler has an external diameter of 13 mm.

Stepper frame support

This was designed to hold the stepper motors intact while in operation. It contains holes that are inter-connected to the stepper's frontal cylindrical section.

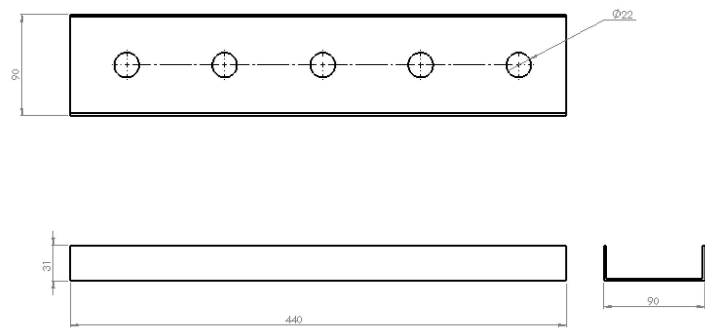


Figure 3.3: Motor holder design

3.1.3 Fabrication and assembly of the active grid system

The fabrication process for the active grid system and test section involved the following steps:

- Frame - The frame was made from mild steel sheets. Four sheets of 1.5mm thickness, 110mm wide and 440mm long are marked and cut using a shearing machine. Holes 20mm diameter for attaching bearings were drilled through two of the sheets. The sheets were then arranged perpendicular to each other, leveled, and welded together to form a hollow cube structure..
- Bearing supports - The bearing holders were made from galvanized aluminum water pipes with an internal diameter of 20mm, which were bored out to 22mm using a lathe machine. These holders were then attached to the frame in alignment with the pre-drilled holes using epoxy adhesive, as welding was not an option for this material. Bearings were force fitted to them as shown in the figure below.

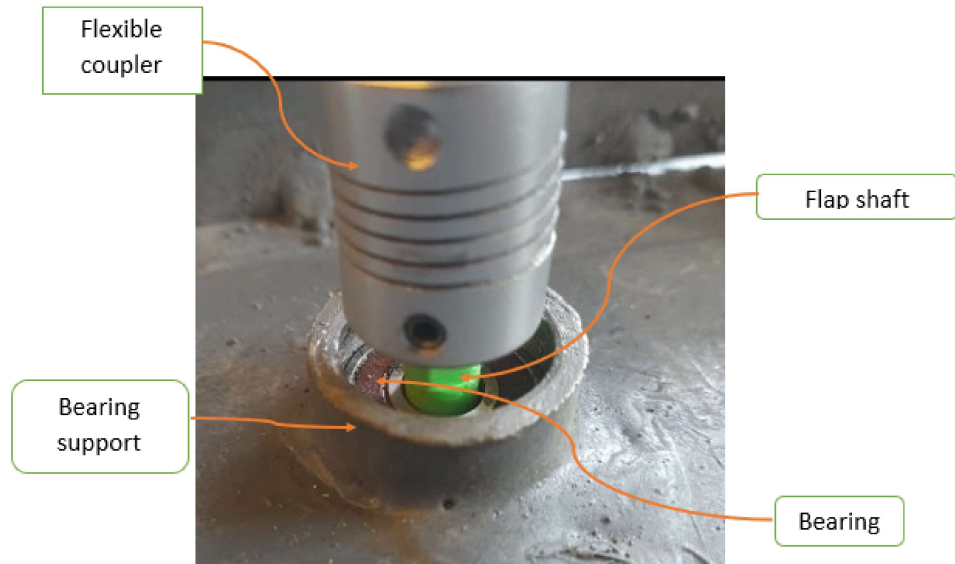


Figure 3.4: Bearing to flap shaft to coupler subassembly

- Test section - The test section was constructed using four 25mm x 25mm x 2mm angle bars, 650mm long, which were cut using an abrasive cutting machine. These bars were welded together at the four corners of the active grid system. At the opposite ends, 50mm x 50mm x 2mm angle bars were used to create flanges, allowing the test section to be bolted securely to the diffuser section of the wind tunnel.
- Flaps - Five flaps, each 435mm long and 85mm wide, were cut from a 5mm thick flat Perspex sheet. The cutting process was done using a laser cutter.



Figure 3.5: Flap and shaft subassembly

- Flap shafts - 3D printed 10 shafts. The shafts were then bonded to the flaps using epoxy adhesive.



Figure 3.6: Flap shaft

- Stepper housing

A 2mm thick mild steel sheet, measuring 85mm wide and 436mm long, was cut using a shearing machine. The positions for the motors were marked on the sheet, and five 22mm diameter holes were drilled. Additionally, 4mm holes were marked and drilled around the larger holes to facilitate motor attachment to the housing.

On the frame, 4 mild steel rectangular tubes of dimensions 20mm by

40mm by 50mm were cut using abrasive cutting machine and each a hole of 60mm was drilled at the width section to attach the stepper holder sheet.

- They were welded to the frame at the 4 different corners to provide rigid support to the holder.
- The transparent casing was fabricated through cutting 5 pieces of 6mm thick perspex using the circular saw bench machine. The edges of the perspex were polished to remove any roughness or burrs. They were then bonded together using epoxy rigidly to form an open cuboid.



Figure 3.7: Top frame for attaching stepper support



Figure 3.8: Stepper motors attached to stepper holder

3.1.4 Active grid system subassembly

To assemble the components, the flap shafts were fixed at one end of the flaps and connected to the flexible couplers through the frame and bearings.

The bottom shafts were attached only to the bearings. The stepper motors were bolted to the motor holder. After aligning the motor shafts with their corresponding couplers on the frame, the stepper holder was bolted to the four support tubes, and the motor shafts were securely tightened to the couplers. Lastly, the transparent casing was carefully fitted to enclose the stepper motor holder and motors

3.1.5 Design considerations of the test rig

1. Highly rigid structure: The structure should have very little to no deformation under load.
2. Minimal interference to airflow: The design should incorporate shapes with minimal obstruction to the airflow
3. The design should allow for the load cell to be positioned in such a way that it captures all relevant forces while remaining unobtrusive to the airflow.
4. Half the length of the test section

3.1.6 Design of the test rig structure

The maximum theoretical force exerted on the test rig is equivalent to the maximum drag force that will be felt on a parachute during the test. This maximum drag force is calculated as follows:

We will first consider the largest diameter which a parachute can have within the current test section which is 440mm by 440mm.

Taking the diameter as $D = 0.44\text{ m}$, the area A is computed using the formula:

$$A = \frac{\pi D^2}{4} \quad (3.4)$$

Thus, the maximum area is approximately 0.1521143 m^2 .

To calculate the drag force F_d , we use the formula:

$$F_d = \frac{1}{2} C_d \rho A v^2 \quad (3.5)$$

Given the following values:

- Drag coefficient, $C_d = 1.54$
- Density, $\rho = 1.225\text{ kg/m}^3$
- Area, $A = 0.1521143\text{ m}^2$
- Maximum flow velocity, $v = 21\text{ m/s}$

The drag force is approximately 63.28 N.

This drag force will act on the test rig as it would a point load on a cantilever.

The deflection (δ) at the free end of a cantilever beam under a point load (F) is given by:

$$\delta = \frac{F \cdot L^3}{3 \cdot E \cdot I} \quad (3.6)$$

where:

- F is the applied force (63.28 N).
- L is the length of the beam (220 mm = 0.22 m).
- E is the modulus of elasticity of the material.
- I is the second moment of area for a circular cross-section, given by

$$I = \frac{\pi \cdot d^4}{64} \quad (3.7)$$

To have a "zero" deflection, we set δ to an extremely small value, close to zero. For practical purposes, let $\delta = 1$ mm (0.001 m):

$$d = \left(\frac{43.123548}{3 \cdot \pi \cdot E \cdot 0.001} \right)^{\frac{1}{4}} \quad (3.8)$$

Calculating d for different Materials:

Table 3.3: Minimum Rod Diameters for Small Deflection

Material	E (Pa)	Minimum Diameter d (mm)
Aluminum (Al)	69×10^9	16
Mild Steel	210×10^9	13
ABS Plastic	2.1×10^9	38
Stainless Steel	200×10^9	14

The smaller the diameter, the lower the nominal area, and consequently, the lower the drag induced in the flow. Based on the comparison of minimal

diameters in Table 3.3, a mild steel rod with a 13mm diameter was chosen because it has the smallest diameter.

The test rig rod design is designed to accommodate the load cell sensor attachment as shown in Figure 3.9.

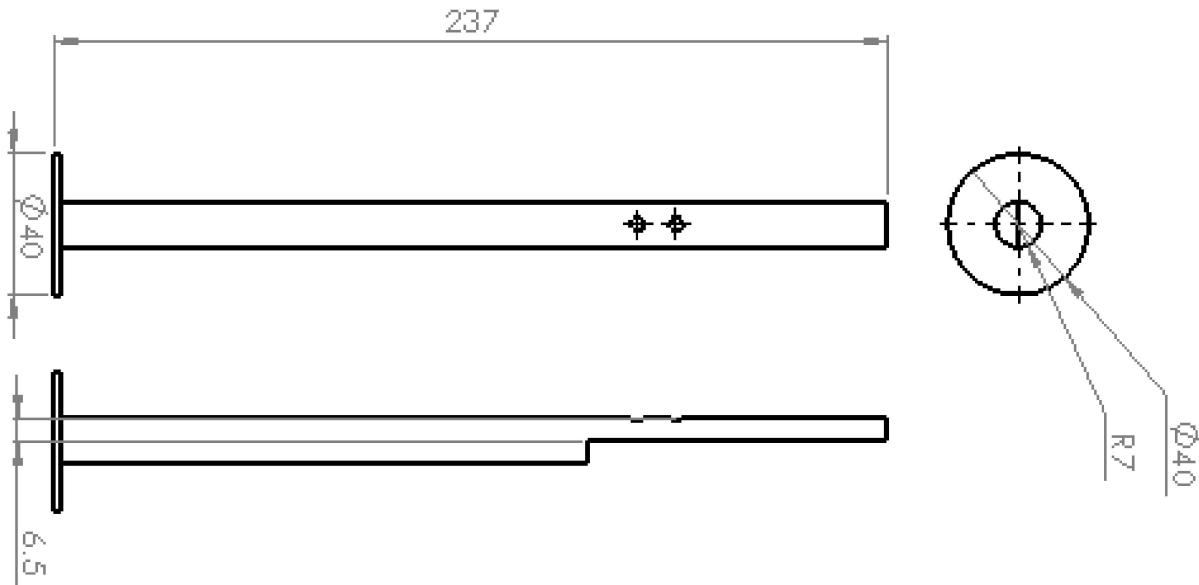


Figure 3.9: Test rig design

3.1.7 Fabrication of test rig

- Design changes

Due to the standardization and availability of round bars, the test rig was modified to use a standard 16mm diameter aluminum rod, as this was the closest standard size available locally. The originally specified mild steel was not available in smaller dimensions like those in the design.

- The fabrication process

The process involved the following steps: One end of the test rig was marked, and the curved surface was cut along the diametral axis using a vertical milling machine. Two holes were then drilled into the milled profile to allow for the attachment of the load cell. Afterward, deburring was done to remove any rough chips. One end of the load cell was bolted securely to the test rig using M3 bolts



Figure 3.10: Test rig

3.1.8 Parachute design

The parachute design process adopted in this project is adapted from LabRat Scientific's guidelines , which provide a structured approach to calculating the necessary parameters for a functional parachute.

Parachute design considerations

1. **Suspended rocket weight:** This is the weight of the rocket specifically at apogee. This weight is calculated by subtracting the fuel weight from the total weight of the rocket whereby, the total weight of the rocket is 26 kg, and the fuel weight is 6 kg. Therefore, the

suspended weight is determined to be 20kg.

$$\text{Mass at apogee} = \text{Total Mass} - \text{Fuel Mass} \quad (3.9)$$

$$\text{Mass at apogee} = 26 \text{ kg} - 6 \text{ kg}$$

$$= 20 \text{ kg}$$

2. Shape considerations: Next, the desired shape of the parachute was selected. A hemispherical shape was chosen for both the drogue and the main parachute for its high drag coefficient and ease of fabrication. This ensures that the parachute can be reliably produced and deployed, making it a practical choice for the project. The material selected for the parachutes was Ripstop Nylon due to its durability and suitability for parachute applications.

- Drogue Parachute: Hemispherical (Ripstop Nylon)
- Main Parachute: Hemispherical (Ripstop Nylon)

3. Theoretical drag coefficient: The drag coefficient(C_d) for a hemispherical parachute was selected based on theoretical data. A value of 1.54 is used, which is a standard coefficient for hemispherical parachutes.

- $C_d = 1.54$

4. Desired impact velocity: A terminal velocity of 21 m/s was chosen for the drogue parachute, and 5.5 m/s for the main parachute as regulated by the Spaceport America Cup regulations. The desired impact

velocity was determined based on the need to avoid damage to the rocket and minimize wind drift.

- Terminal velocity for drogue: 21 m/s
- Terminal velocity for main: 5.5 m/s

5. The canopy area: This dictates the nominal area required to achieve the desired terminal velocities. The canopy area(A) is calculated using the following drag force equation:

$$A = \frac{2mg}{\rho v t^2 Cd} \quad (3.10)$$

There are 2 types of parachutes to be constructed including a mini(drogue) and the main parachute as described below:

(a) Drogue Parachute

This is the smaller parachute that stabilizes the payload and provides an initial deceleration of approximately 21m/s before the deployment of the main parachute.

Drogue parachute calculations

Drogue parachute design constraints are:

$$m = 20\text{Kg}, g = 9.81 \text{ m/s}^2, \rho = 1.225 \text{ kg/m}^3, V_t = 21 \text{ m/s} \quad Cd = 1.54.$$

- Canopy area

Substituting to equation 3.6,

$$A = 0.471m^2$$

- Diameter

To find the diameter D from the area A of a circle, we use the formula:

$$D = \sqrt{\frac{4A}{\pi}} \quad (3.11)$$

Substituting the value of A , we find the diameter is approximately 0.774 m.

- Spill hole Area and diameter

This is the aperture hole that increases the stability of the rocket during descent. The spill hole also known as apex vent area is 1% of the nominal area is sufficient as the standard used in the previous parachute model [4]:

Given $A = 0.471 \text{ m}^2$, we can find 1% of A :

1% of A is 0.0047 m^2

Spill hole diameter is found by substituting to equation 3.7.

$$D = 0.244 \text{ m}$$

- Number of Gores

$$\text{Number of Gores} = \frac{\text{Circumference}}{\text{Gore Width}} \quad (3.12)$$

The circumference (C) of the drogue parachute knowing its diameter is:

$$C = \pi \times D \quad (3.13)$$

Substituting D,

$$C = \pi \times 0.244\text{m}$$

$$\therefore C = 2.43\text{m}$$

Recommended Gore Width is between 20cm - 50cm]. Selecting a gore width of 30cm, which is at the midpoint of the recommended range gives,

Substituting to equation 3.9.

$$\text{Number of Gores} \approx \frac{2.4}{0.3}$$

$$\text{Number of Gores} \approx 8\text{Gores}$$

Table 3.4: Drogue parachute summary table

Canopy area	0.47m ²
Canopy diameter	0.77 m
Canopy circumference	2.433m
Spill hole area	0.0047m ²
Spill hole diameter	0.244m
Gores	8

(b) Main Parachute

This is the parachute that provides primary deceleration to slow the payload down to a survivable impact velocity of approximately 5.5m/s.

Main parachute calculations

The main parachute design constraints are:

$$m = 20\text{Kg}, g = 9.81\text{m/s}^2 \rho = 1.225\text{Kg/m}^2 Vt = 5.5\text{m/s}, Cd = 1.54.$$

- Canopy Area

Substituting to equation 3.6,

$$A = 6.86\text{m}^2$$

- Diameter

To find the diameter D from the area A of a circle, we use the formula:

$$D = \sqrt{\frac{4 \times 6.86 \text{ m}^2}{\pi}}$$

Calculating the diameter:

$$D \approx 2.95 \text{ m}$$

Thus, the diameter is approximately 2.95 m.

- Spill hole Area and diameter

The spill hole also known as the apex vent area is 1% of nominal area:

Given $A = 6.86 \text{ m}^2$, we can find 1% of A : Substituting the value of A :

$$1\% \text{ of } A = 0.01 \times 6.86 \text{ m}^2$$

Therefore, 1% of A is approximately 0.068 m^2

Spill hole diameter is found by substituting to equation 3.7.

$$D = 0.295\text{m}$$

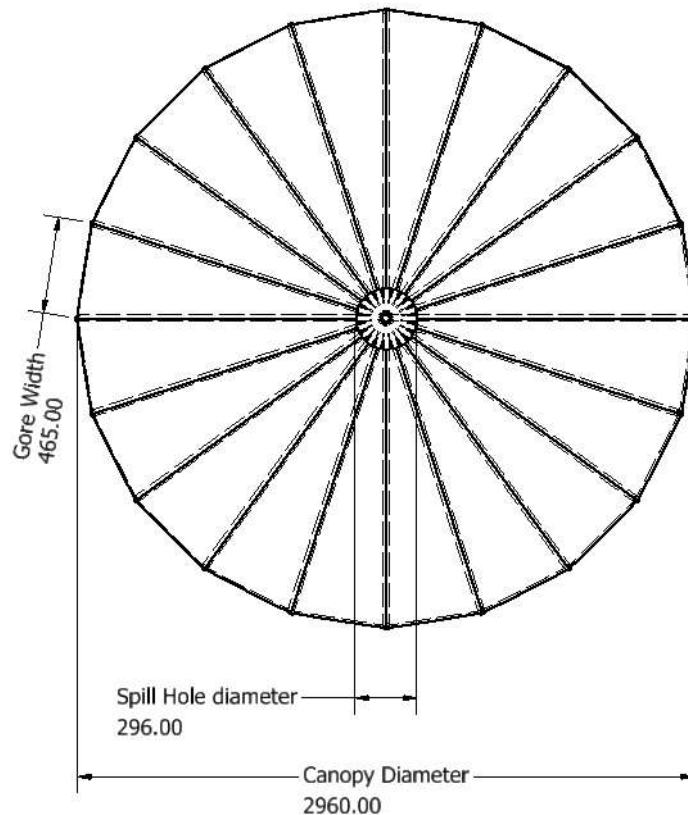


Figure 3.11: Main Parachute Canopy design-Top View

- Number of Gores

The circumference (C) of the main parachute is:

$$C = \pi \times D$$

$$\therefore C = 9.29\text{m}$$

Recommended Gore Width is between 20cm - 50cm. A larger gore width is selected for ease of fabrication.

Selecting a gore width of 46.5cm which is at the upper limit of the recommended range and considering the symmetry and ease of construction it gives,

Substituting to equation 3.9.

$$\text{Number of Gores} \approx \frac{9.29}{0.46}$$

$$\text{Number of Gores} \approx 20 \text{ Gores}$$

Table 3.5: Main parachute summary table

Canopy area	6.86m ²
Canopy diameter	2.95 m
Canopy circumference	9.29 m
Spill hole area	0.068m ²
Spill hole diameter	0.295 m
Gores	20

6. Shock cord design

(a) Design Calculations

The first step in designing the shock cord was to calculate the opening shock load that the parachute system would experience upon deployment. This load is critical to ensure that the shock cord can withstand the forces without failing

- i. Drogue and main parachute Opening Shock Load The opening shock forces are critical for understanding the loads experienced during parachute deployment. It is calculated using the Pflanz Method, which is expressed as:

$$F_x = (S \cdot C_D)_p \cdot q \cdot C_x \cdot X_1 \quad (3.14)$$

where:

- F_x : Opening shock force
- $(S \cdot C_D)_p$: Effective drag area, given by $S \cdot C_D$
- q : Dynamic pressure, calculated as
- C_x : Empirical opening force coefficient
- X_1 : Force reduction factor, determined from empirical charts

Additional formulas used:

- Parachute surface area:

$$S = \pi \cdot \left(\frac{D}{2} \right)^2 \quad (3.15)$$

- Inflation time:

$$t_f = \frac{n \cdot D_0}{v_1} \quad (3.16)$$

- Ballistic parameter:

$$A = \frac{2 \cdot W_t}{(S \cdot C_D)_p \cdot \rho \cdot g \cdot v_1 \cdot t_f} \quad (3.17)$$

Parameters and Results

The following table summarizes the parameters used and the resulting opening shock forces for both the main and drogue parachutes:

Table 3.6: Parameters and Opening Shock Forces for Main and Drogue Parachutes

Category	Main Parachute	Drogue Parachute
Shared Parameters		
Drag coefficient C_d	1.54	1.54
Empirical coefficient C_e	1.7	1.7
Dynamic pressure q (Pa)	270.115	270.115
Rocket weight W_r (N)	196.2	196.2
Specific Parameters		
Inflation time t_i (s)	0.207	0.118
Parachute diameter D (m)	2.9	0.774
Surface area S (m^2)	6.6	0.47
Force reduction factor X	0.99	1.0
Results: Opening Shock Force		
Opening shock force F_o (N)	4618	336.49

The calculated opening shock force for the main parachute was approximately **4618 N**, while the drogue parachute experienced a significantly lower force of **336.49 N**. This difference primarily corresponds to the drogue parachute being used for sta-

bility and controlled descent, whereas the main parachute is responsible for full deceleration

ii. Cord Dimensions and Strength

To ensure the shock cord can withstand the calculated forces, the following dimensions were considered:

Table 3.7: Shock Cord Dimensions and Strength

Thickness	Width	Breaking Weight
0.08" (2.032 mm)	5/8" (15.875 mm)	1500 lbs (680 kg)
-	1.25" (31.75 mm)	3200 lbs (1450 kg)

The 5/8-inch (15.875 mm) width was selected as it can withstand the opening shock. Additionally, cord ties are considered to further decrease the opening shock of 470Kgf.

(b) Length Design

The length of the shock cord was designed considering the following factors:

- **Stretch Factor (T):** Tubular Nylon has a stretch factor between 10% to 30%. For this design, 20% was chosen.
- **Max Rocket Length (L_r):** The maximum rocket length during descent is 2 meters.
- **Cord Length (L_o):** The cord length was determined to be 4 times the rocket length:

$$L_o = 4 \times L_r = 4 \times 2 = 8 \text{ meters}$$

- **Final Length Considering Stretch:**

$$L_{\text{final}} = T \times L_o = 1.25 \times 8 = 10 \text{ meters}$$

This final length ensures that the shock cord can safely absorb the forces during deployment while accounting for stretching under load.

(c) Material Selection

The shock cord is designed with two distinct sections, each serving a specific purpose:

- **Lower Section (50mm):** Made of **Kevlar**, chosen for its high-temperature resistance, protecting the upper nylon cord from the ejection charge.
- **Upper Section (8000mm):** Made of **Tubular Nylon**, selected for its ability to absorb the opening shock and prevent damage to the parachute canopy.

3.1.9 Model parachute design

The model parachute was designed to replicate the aerodynamic behavior of the full-scale hemispherical parachute, scaled down to fit within the wind tunnel's test section.

Design considerations:

1. The model parachute should be designed to fit within the wind tunnel's 440mm x 440mm x 650mm test section

2. The model parachute should be scaled down from the full-size parachute diameter of 2.95m.
3. The model parachute should be scaled down from the full-size suspension line length of 4.425m.
4. The model parachute should have a maximum blockage ratio of 10% of the cross-section area.

To achieve a blockage ratio of 10%, the parachute's projected area should be:

$$\text{Area of model parachute} = 10\% \times \text{Cross section area of test section} \quad (3.18)$$

$$10\% \times (440 \text{ mm} \times 440 \text{ mm}) = 19360 \text{ mm}^2$$

$$\therefore \text{maximum Model diameter} = 157 \text{ mm}$$

$$\text{Model spill hole diameter} = 15.7 \text{ mm}$$

$$\text{Scale factor} = \frac{\text{Model diameter}}{\text{Full size diameter}} \quad (3.19)$$

$$\text{Scale factor (S.f)} = \frac{0.157 \text{ m}}{2.95 \text{ m}} = 0.05322$$

$$\text{Model suspension lines} = \text{S.f} \times 4425 \text{ mm} = 235 \text{ mm}$$

3.1.10 Parachute fabrication

- Design modifications

Due to the unavailability of the originally intended parachute fabric

locally, tear-resistant nylon cloth was selected as an alternative. Although it is less reliable than Ripstop Nylon for this application, it is capable of withstanding the drag forces experienced by the rocket, making it a suitable replacement

- Fabrication process

The fabrication process involved cutting the cloth into the required gores with precise dimensions. The pieces were then sewn together, incorporating cords between the gores. The circumference along the nominal area diameter was also reinforced to enhance reliability and reduce the risk of tearing. The parachute fabrication was outsourced to a local tailor. Figure 3.12 shows the model parachute.



Figure 3.12: Fabricated model parachute

3.2 Electrical circuit design

The design of the electrical and electronic modules of the active grid system is divided according to the following subsections:

1. Motor selection and sizing
2. Sensors
3. Power supply selection

The electrical module design is expected to provide electrical power to various electrical components throughout the project. This design also facilitates the transmission of electrical signals between the components. The components to be powered are: the microcontroller, motors and their drivers, sensors, amplifiers, and ADC converter. The module allows the microcontroller unit to get data from the sensors. It also allows for the transmission of control signals from the microcontroller to the actuators.

3.2.1 Motor selection and sizing

The following are considered:

1. Torque: The motor should have enough torque to overcome the load, accounting for both static and dynamic loads.
2. Positioning accuracy: Should be able to allow for fine adjustments.

3. Compatibility with Arduino and simple control
4. Cost and availability: The selected motor must fit within the project budget and be readily available

Based on the requirements of high holding torque, precise positioning, and simple control, a stepper motor was chosen over servo, DC, and AC motors.

3.2.2 Stepper Motor consideration

The maximum torque required to be overcome can be calculated using the equation

$$T = q \cdot A \cdot d \quad (3.20)$$

where

- q is the dynamic pressure,
- A is the area of the flap when perpendicular to airflow,
- d is the distance from the axis of rotation

For this application:

$$T = 270.115 \text{ Pa} \times (0.085 \text{ m} \times 0.440 \text{ m}) \times 0.0425 \text{ m}$$

Substituting the values, we get:

$$T = 270.115 \times 0.0374 \times 0.0425 = 0.4294 \text{ Nm}$$

This torque value represents the fully closed position of the flap, where the torque demand is at its maximum. Based on the calculated torque (0.4294NM), a NEMA 17 stepper motor was chosen.

3.2.3 Stepper motor driver

A stepper system performance is dependent not only on the motor but also on the stepper driver. Stepper driver considerations:

1. Should enable easy interface with a microcontroller.
2. Should have an output capacity greater than 3.2 V.
3. Should have inbuilt safety functions like under-voltage lockout, and over-temperature
4. Should have a small step pulse duration

The considered motor drivers are DRV8825 and A4988. DRV8825 driver has been chosen for this project due to its availability.

3.2.4 Limit switches

Limit switches are used to halt flap rotation when they align parallel to the airflow, ensuring stable laminar conditions for measurements before initiating turbulence generation.

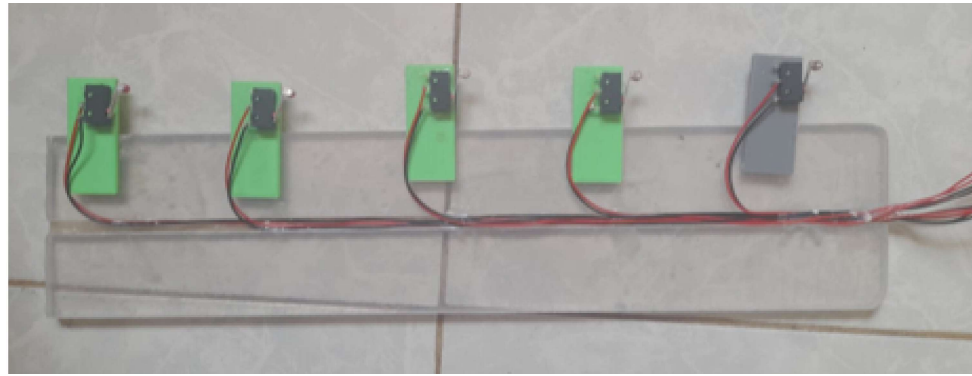


Figure 3.13: Limit switch

3.2.5 Sensors

1. Pitot tube is used to measure the dynamic pressure of the airflow in the wind tunnel, which can be related to the flow velocity thus determining the turbulence levels. It's a simple and reliable tool for providing accurate measurements of airspeed. This makes it essential to understand the effect of different turbulence levels on the parachute. Pressure sensor MPXV7002DP chip is used in conjunction with the pitot tube for accurate readings
2. A load cell measures the drag force acting on the parachute system.
The design considerations are:
 - (a) Compatibility with the expected velocity range
 - (b) Suitable response time for capturing rapid changes in flow
 - (c) Force range and sensitivity
 - (d) Durability and ease of calibration

- (e) Integration with selected data acquisition system
- (f) Small cross-section area that is less than the test rod diameter
- (g) Can measure 60 N and above

A 10kgf, 5V, 0.0015A loadcell measuring 12.7mm by 12.7mm by 80mm was chosen.

3.2.6 Power Budget

In order to choose the correct power supply, a power requirements calculation table was created. The table 3.8 shows how the current draw and power consumed by each component. Taking an efficiency rate of 80% the

Table 3.8: Power requirements for the components in the active grid system.

Component	Voltage (V)	Current (A)	Power (W)	Quantity	Total Power (W)
Nema 17	3.2	2	6.4	5	32
Stepper Driver	5	2	10	5	50
Loadcell	5	0.0015	0.0075	1	0.0075
Pitot tube	5	0.3	1.5	1	1.5
Pressure sensor	5	0.025	0.125	1	0.125
Arduino mega	5	0.16	0.8	1	0.8

total power required is 106W.

$$\text{Efficiency}(\eta) = \frac{\text{Total Power Required}}{\text{Power Supplied}} \times 100\%$$

Assuming $\eta = 80\%$,

$$PowerSupplied = \frac{\text{Total Power Required}}{\eta} \quad (3.21)$$

$$\therefore \text{Power Supplied} = \frac{100.83}{0.8} \\ = 106\text{W}$$

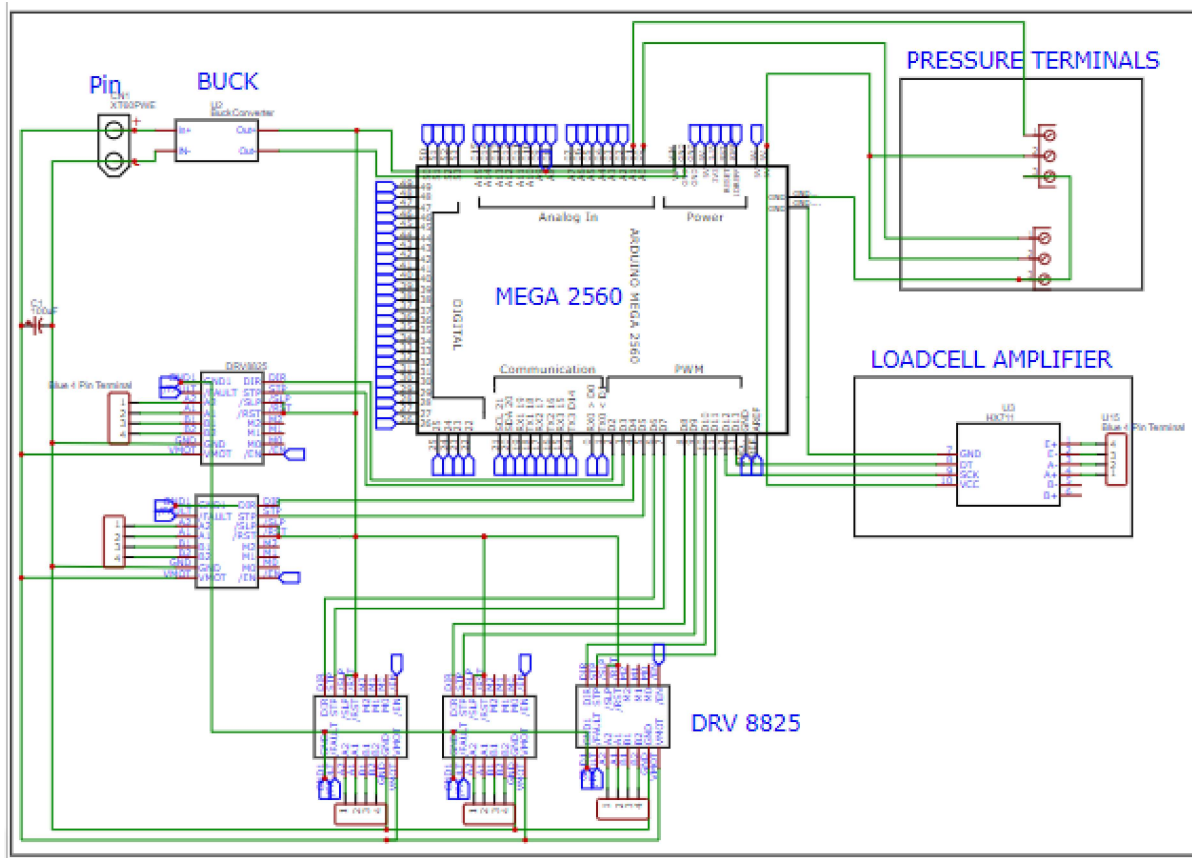


Figure 3.14: Electrical circuit design

3.2.7 Electrical circuit fabrication

The electrical circuit fabrication involved assembling various components on a perforated board. These included DRV8825 motor drivers attached to female header pins soldered onto the board, RGB status LEDs with $1\text{k}\Omega$ resistors, JST 2-pin connectors for limit switches, 4-pin right-angle plug-gable terminal blocks for stepper motor connections, a $100\mu\text{F}$ capacitor, a 3-pin terminal block for the Pitot sensor, a step-down buck converter to reduce 12V input to 5V, an HX711 load cell amplifier, an XT60 connector for the 12V power input, and an Arduino Mega mounted on female header pins soldered to the board.

These connectors facilitated quick assembly and disassembly, simplifying troubleshooting and component replacement.

The board was segmented into distinct sections to manage power requirements effectively. A high-powered section operated at 12V, while a low-powered section operated at 5V. Components were soldered to their designated sections, illustrated in figure 3.15, to ensure safe and efficient integration.

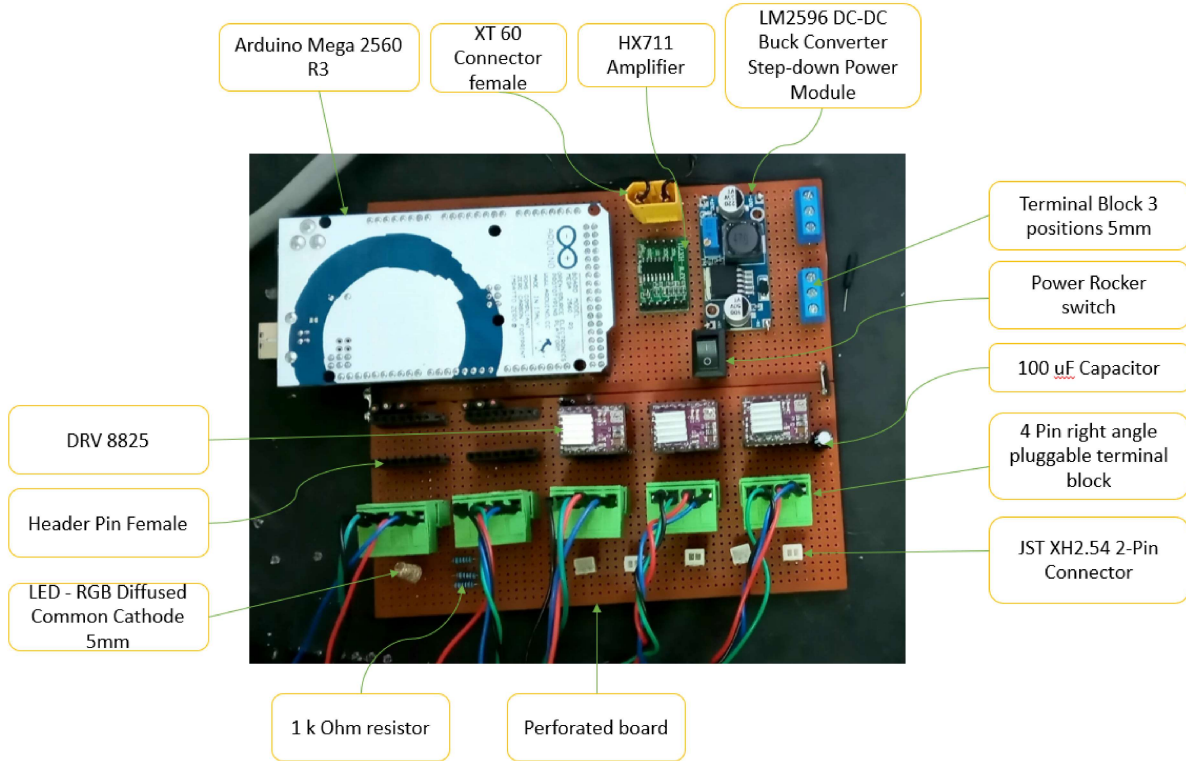


Figure 3.15: Fabricated electrical circuit

3.2.8 Instrumentation setup

The instrumentation setup, illustrated in figure 3.18, included a load cell and a Pitot tube (figure 3.16) for data collection. The load cell was mounted on the test rig using M3 bolts . The Pitot tube was mounted on the test rig with connections routed to the data acquisition system. Wiring and connectors were soldered and insulated to ensure reliable signal transmission. Calibration validated the accuracy of both instruments before experimentation.

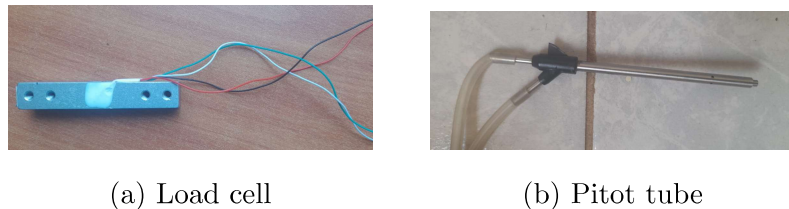


Figure 3.16: Sensors used

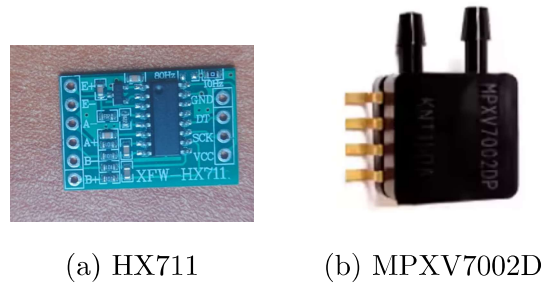


Figure 3.17: Interface modules

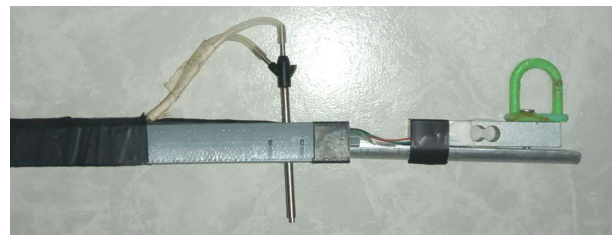


Figure 3.18: Instrumentation setup

3.3 Control module design

When selecting a control module for the active grid system, several factors were taken into account, including the processing power, availability of sufficient I/O pins, and cost.

3.3.1 Micro-controller selection

Below is a comparison of different micro-controllers considered for the project:

- Arduino Mega2560: Offers 54 digital I/O pins, 16 MHz processing speed, 8 KB RAM, and operates at 5V with a power consumption of 0.5W.
- Arduino UNO: Provides 14 digital I/O pins, which may be insufficient for more complex control needs.
- ESP32: Features 48 I/O pins and more advanced processing capabilities, but it may be overkill for this application.
- Raspberry Pi: Has 26 GPIO pins and offers high processing power, but the added complexity and power requirements might not be necessary.

Given the specific requirements of the project, the Arduino Mega2560 was selected for its sufficient number of I/O pins, adequate processing power, and cost-effectiveness.

3.3.2 Software Implementation

Arduino IDE was chosen as the development environment due to its compatibility with the selected microcontroller, ease of use, and community support. Pycharm environment was also selected for data analysis and visualization using Python programming language.

- The Arduino C++ code controlled the five stepper motors and collected sensor values for real-time feedback. Each motor was assigned specific pins and programmed for randomized operation based on the experimental round. Simulated sensor data, including drag force, velocity, and drag coefficient, were displayed on the Serial Monitor at regular intervals for real-time monitoring.
- The Python code processes real-time data from the Arduino, enabling visualization and logging. Using the pyserial library, data is received, parsed into variables (drag force, velocity, and drag coefficient), and dynamically displayed through matplotlib graphs. The data is also saved to a CSV file for offline analysis. The script includes error handling for serial connection issues, ensuring uninterrupted operation until terminated.

3.4 CFD Simulation

CFD simulations were carried out using Ansys Fluent to model the air-flow around the parachute. These simulations were conducted to predict drag forces, visualize flow patterns, and to compare with experimental and analytical results.

3.4.1 Simulation Setup

The simulations used the SST $k-\omega$ turbulence model, chosen for its accuracy in capturing boundary layer separation and flow behavior around the complex objects. The inlet velocity was set to 21 m/s, matching the wind tunnel conditions, with a pressure outlet applied to maintain system balance.

3.4.2 Geometry and Mesh

The parachute geometry and test rig was modeled to match the exact dimensions and relative distances calculated in subsection 3.1.9. The surrounding air domain was defined as 440mm x 650mm to match the test section. Meshing, illustrated in figure 3.19, was performed with an element size of 5.322mm.

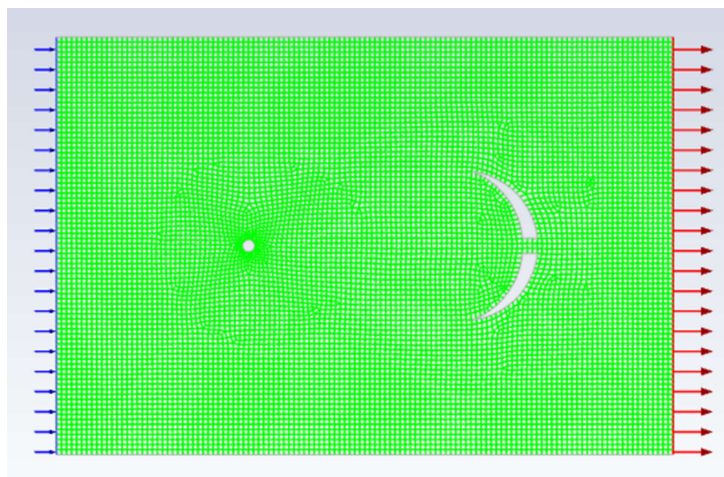


Figure 3.19: Mesh generated for CFD simulation of the parachute geometry

3.4.3 Boundary Conditions

The parachute surface was modeled as a solid using boolean subtraction tool. The wall was modeled as a no-slip wall to replicate real-world conditions.

3.4.4 Validation of CFD model

Validation of the CFD model was performed by simulating the full-scale main parachute. The results were compared to analytical calculations of the drag force. Using equation 3.5, the analytical drag force was calculated to be 2857.388 N, while the simulated drag force, illustrated in figure 3.20, converged to 2500 N. The close match between these results confirms the reliability of the simulation setup.

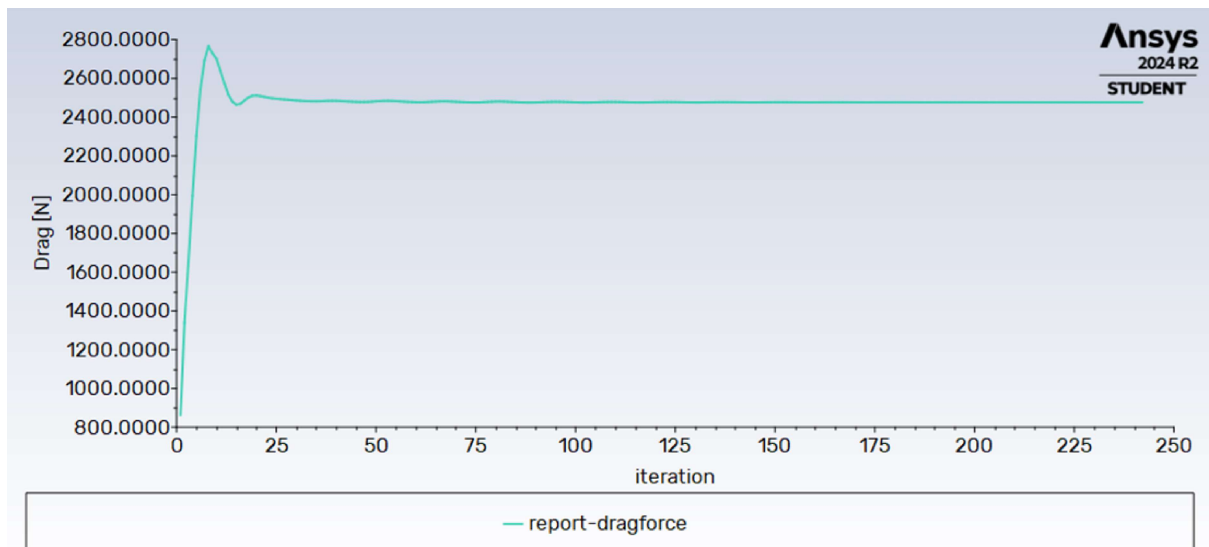


Figure 3.20: Simulated drag force of the full scale parachute

3.4.5 Post-Processing and Analysis

Post-processing involved analyzing drag force, velocity contours, and pressure contours, around the parachute.

4 Results and Discussion

This chapter presents the results from the design, fabrication, and testing of the active grid system and model parachute. It covers mechanical, electrical, control modules and data from wind tunnel tests, circuit performance, and simulations, comparing experimental and simulated results.

4.1 Mechanical Module

The system was designed and built to meet the experimental requirements for turbulence generation, drag force measurement, and data collection. It consists of a test section, an active grid system (AGS), and instrumentation. The design focused on structural integrity, flow uniformity, and adaptability for different test configurations. The frame and test section were made of mild steel to ensure durability and resistance to deformation under operational loads. Perspex sheets were used for the test section walls to allow visual observation while minimizing flow interference. The AGS, consisting of Perspex flaps, bearings, and flexible couplers, was integrated into the tunnel to generate controlled turbulence. A 2D CAD model, shown in Figure 4.1, provides a detailed representation of the major components and system dimensions. The initial assembly of the active grid system and test section subassembly is shown in figure 4.2 below

The 2D view of the designed CAD model, presented in Figure 4.2, provide a comprehensive representation of all the major components assembly with

the major dimensions of the system.

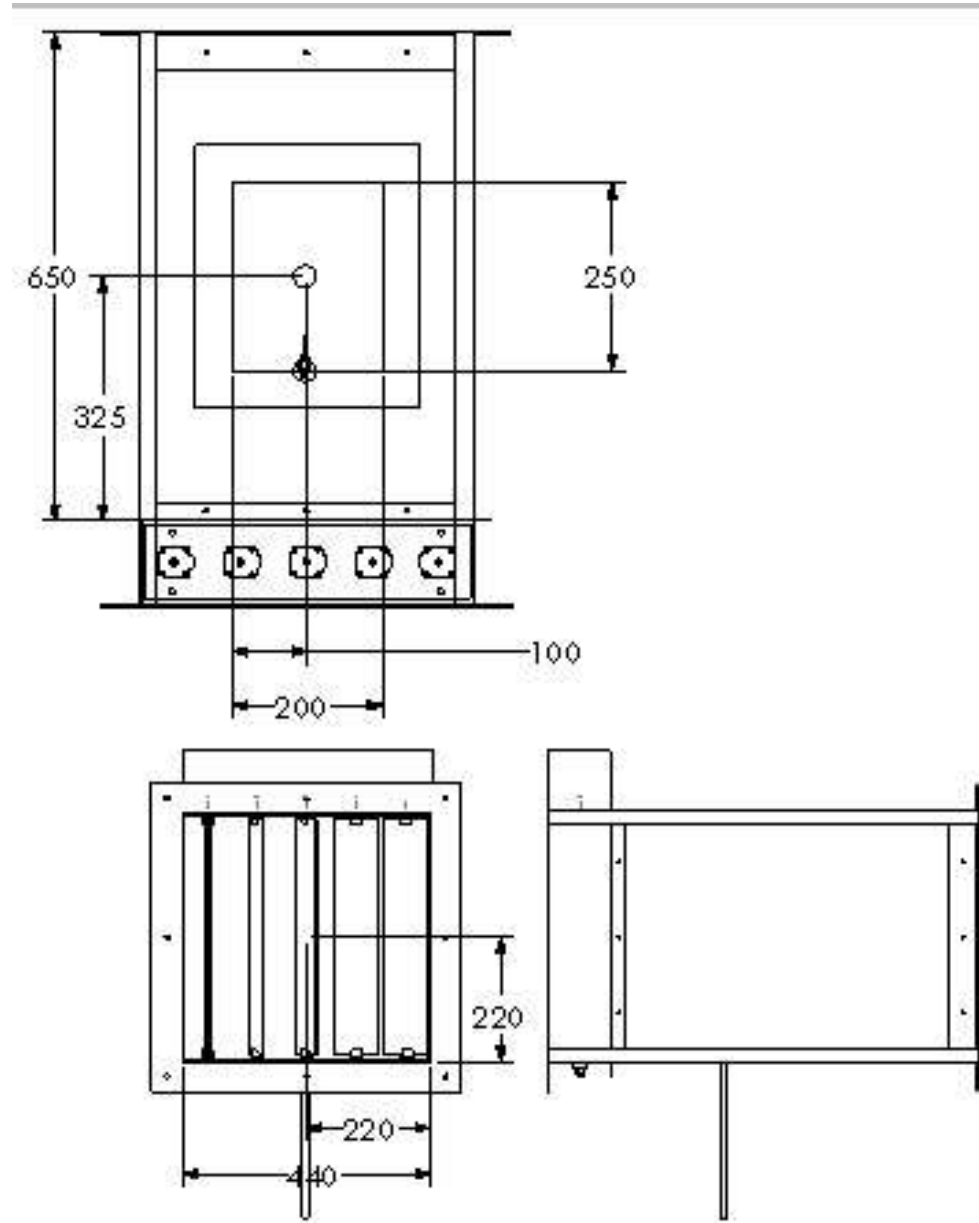


Figure 4.1: 2D drawing of AGS and test section

The 3D views of the designed CAD model, presented in Figure 4.2, provide a comprehensive representation of all the major components of the Active grid system.

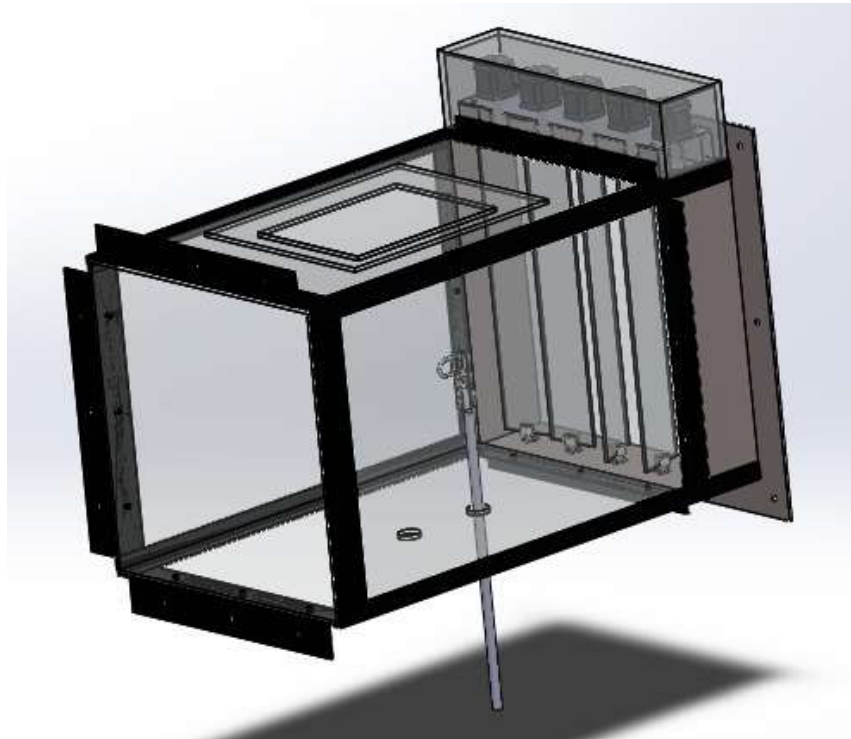


Figure 4.2: 3D model of AGS and test rig

The mechanical design of the active grid system (AGS) ensures precise and reliable turbulence generation, as well as smooth operation of the moving components. The design takes into consideration accessibility and user-friendliness to allow for modularity of tests

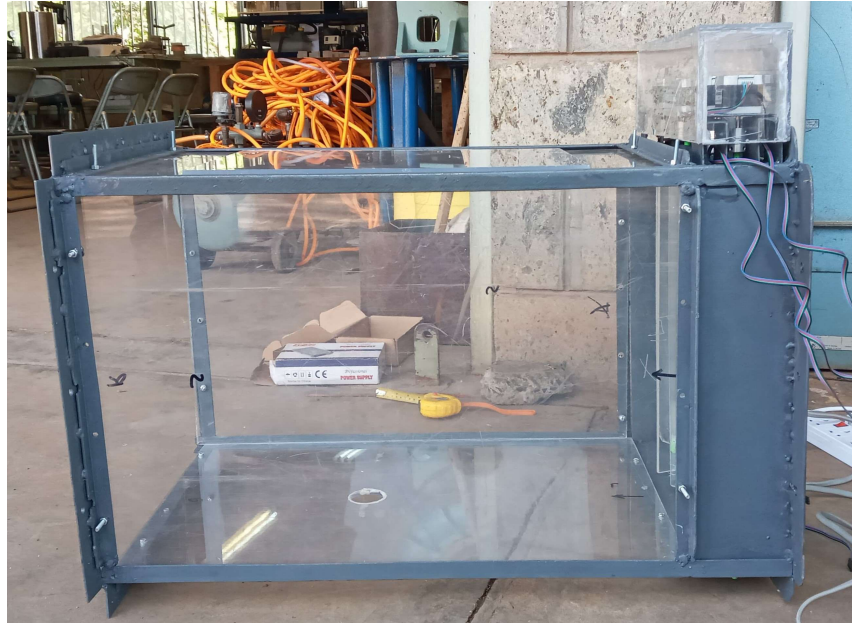


Figure 4.3: Fabricated AGS and test section

4.2 Electrical and Control Systems

The electrical module was fabricated with specific components carefully chosen to meet the power requirements of the system. The system is powered by a 240V to 12V power supply module, with the circuit soldered onto a prototyping board hence stability and maintenance ease. Five NEMA 17 motor are employed for the flap actuation mechanism. This ensures accurate motion during generating turbulence. These motors are driven by DRV8825 drivers thus optimal performance. The motors draw a current of 1.4A each resulting to 7A total current drawn. The HX711 is driven by a buck converter which steps down the 12V supply to 5V suitable for its voltage requirement. The MPXV7002DP pressure sensor for convert-

ing velocity values is powered by 5V from Arduino 5V supply to ensure consistency of the values achieved. The design of the circuit achieved is as illustrated in figure 4.4 whereas the fabricated circuit shown in figure 4.5

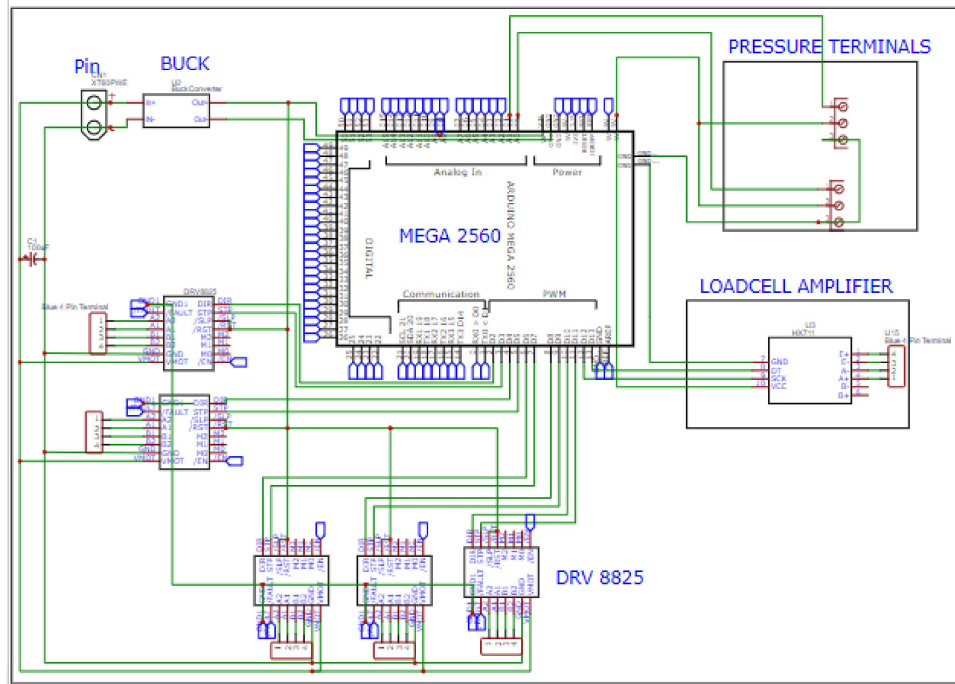


Figure 4.4: Wiring diagram of the circuit

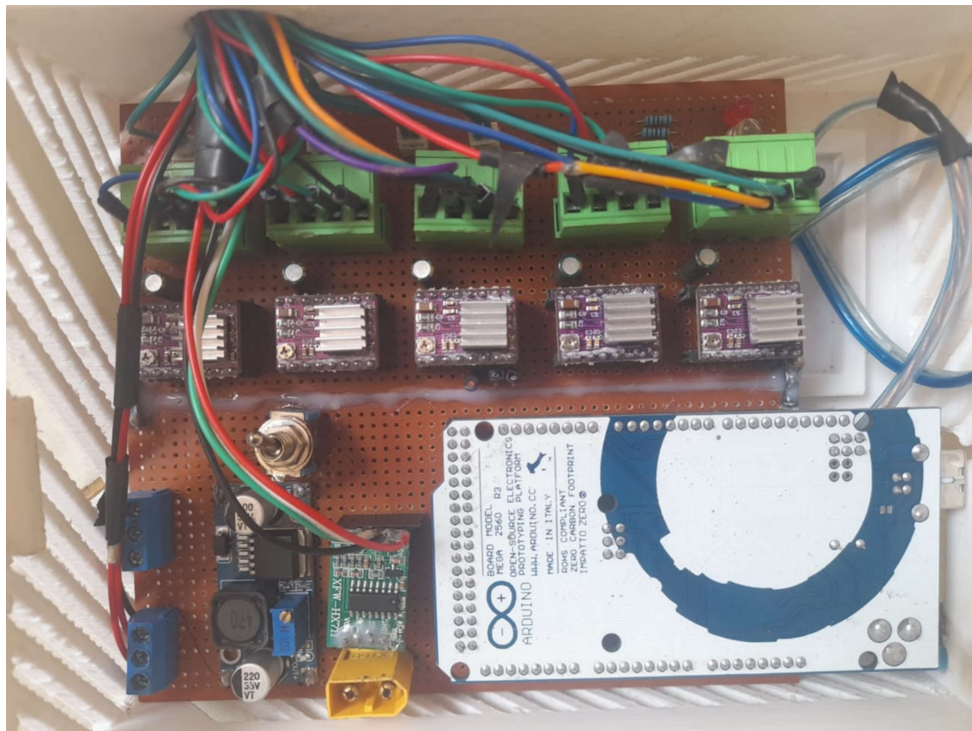


Figure 4.5: Fabricated electronic circuit

4.2.1 Instrumentation System

The instrumentation system was designed to collect data on drag force and velocity for further analysis. It included a load cell for drag force measurement and a Pitot tube with an MPXV7002DP sensor for velocity measurement. These components were securely mounted on a test rig attached from the bottom section of the test section, as shown in figure 4.6. A data acquisition and logging system, programmed in Python, facilitated real-time analysis of the collected data.

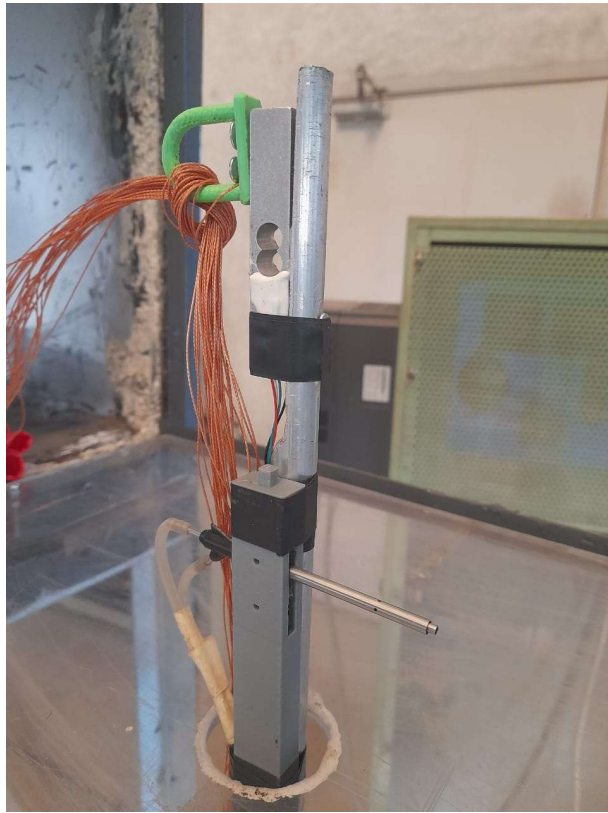


Figure 4.6: Instrumentation setup

The load cell sensor was calibrated using known weights in the lab while the pitot tube was calibrated using hot wire anemometer to ensure accuracy, and their performance was validated. The logging system provided consistent and reliable data during experiments.

4.3 CFD Results

4.3.1 Velocity distribution on model parachute

Figure 4.7 shows the velocity field around the model parachute, simulated in Ansys Fluent. The freestream velocity is uniform upstream of

the parachute, while a significant wake region forms behind it due to flow separation. The highest velocities are observed around the edges of the canopy, where the flow accelerates, while the lowest velocities occur in the recirculation zone. The wake structure indicates turbulence, which is expected for bluff-body aerodynamics.

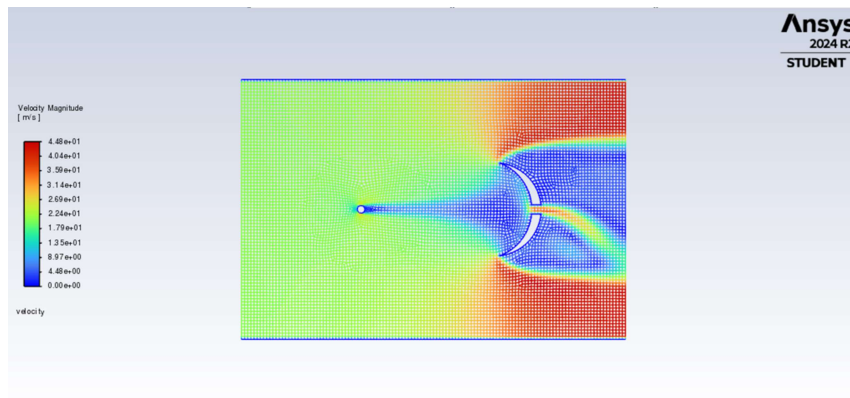


Figure 4.7: Velocity contour plot

4.3.2 Dynamic pressure distribution

Figure 4.8 presents the dynamic pressure contours around the parachute. A high-pressure region forms at the leading edge of the canopy, contributing to the aerodynamic forces. In contrast, the wake region exhibits low pressure, confirming substantial flow separation. The pressure gradient between these regions is a primary factor in the drag force generated by the parachute.

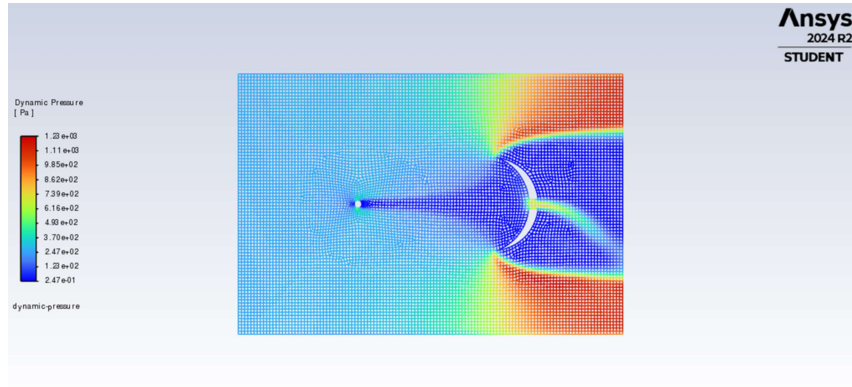


Figure 4.8: Dynamic pressure contour plot

4.4 Testing

The testing phase for the wind tunnel system involved an evaluation of critical parameters of the parachute: the drag force, the flow velocity, their relation to the drag coefficient, tearing effect, and the opening time at both lamina and turbulent flow. The figure 4.9 below indicates the state of the parachute expansion during testing at around 15m/s:



Figure 4.9: Parachute expansion

These play pivotal roles during real environmental deployment of the parachute.

The primary objectives of the tests were to assess the validity of the analytical and simulation values.

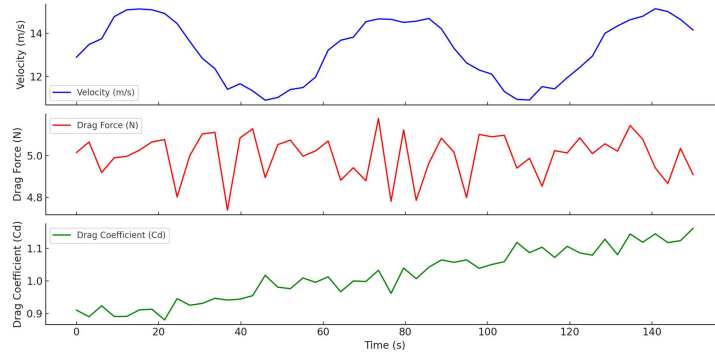


Figure 4.10: Preliminary test showing drag coefficient values at approximately 15m/s

The expected drag coefficient was approximately 1.54, but the recorded values from the preliminary results indicated ranged between 0.88 and 1.15. Therefore the minimum descent velocity it can handle using the drag coefficient of 1.1 and taking weight of rocket to be 20Kg is 4.5M/S which is allowable for the spacePort America cup. However possible reasons suggesting the less accurate results was due to, the load cell or velocity sensor may calibration values were not accurate enough, Variations in turbulence intensity within the wind tunnel could cause deviations from theoretical values and the simplified drag coefficient formula may not fully capture the aerodynamic effects present in the experiment. The material however at higher speeds was rigid enough with some minimal weaknesses along the joints.

4.5 Parachute implementation

Considering the outcomes of the computational fluid dynamics and validation using the experiments done on the model chute, both drogue and main parachutes were successfully implemented according to the design parameters. The table below shows the parameters used to fabricate them:

Table 4.1: Fabrication Details of Main and Drogue Parachutes

Fabrication Parameter	Main Parachute	Drogue Parachute
Number of gores	20	8
Parachute diameter (m)	2.9	0.7
Spill hole diameter (m)	0.24	0.3
Material	Normal Nylon	Normal Nylon
Suspension lines	Present	Present

Figure 4.11 shows the Main parachute and drogue parachute fabricated using the parameters defined in the table 4.1 above.



(a) Drogue parachute

(b) Main parachute

Figure 4.11: Fabricated parachutes

5 Conclusion

The objectives of this project were:

1. To design and fabricate an active grid system structure, a test rig and a robust parachute system for testing in the wind tunnel. 2. To design and develop an electrical circuit for actuation of the active grid system. 3. To implement control algorithms for flow conditioning. 4. To analyze sensor data to extract meaningful information. To this effect, the objectives of this project were successfully achieved through the design, fabrication, and testing of the parachute in the active grid system. The mechanical structure and actuation system of the system were designed to align the flaps parallel to flow, allow data collection and then actuate them in random directions while collecting data for final comparisons. Results showed that NEMA 17 motors provided sufficient torque and speed of actuation. The electrical module demonstrates an acceptable power consumption without deficiencies. Concerning the software, the program actuated the motors as expected allowing correct sensor values measurements. The python environment data analysis system provided a real time monitoring of the drag force, velocity and solved for the drag coefficient intuitively outputting the results in graphs and saving the values in CSV format for future referencing. However a few challenges were encountered:

- There was a considerable deviation between the CFD analysis and the experimental results obtained.

- Limited time for iterative testing and debugging in the wind tunnel.
- Maintaining consistent flow conditions in the wind tunnel to ensure reproducibility
- The suspension lines of the model parachute tended to coil together during testing, resulting in a partially deployed parachute and inconsistent drag force measurements.

This prompted the following recommendations in future research work:

1. A mesh convergence study for the CFD simulation to ensure that the results of a computational simulation are accurate, independent of mesh resolution and reliable.
2. Modification of the flaps using a thinner flaps to ensure minimal blockage area during laminar operations.
3. A more intensive study should be carried on the flow distribution within the test section to determine the best practices for stability of the suspension lines.

References

- [1] E. S. R. A. (ESRA), “Spaceport america cup,” 2025, accessed: 2025-01-26. [Online]. Available: <https://spaceportamericacup.com/>
- [2] ——, “Spaceport america cup: Intercollegiate rocket engineering competition design, test, & evaluation guide,” 2023.
- [3] C. S. A.K. Muchiri, B.Oindi, “Development of a variable test section low speed wind tunnel.” *Proceedings of the Sustainable Research and Innovation Conference JKUAT Main Campus, Kenya*, 2021.
- [4] N. Airframe, *N3.5 Airframe team documentation*. N/A, 2024.
- [5] J. White, “Dynamics of parachute mounting systems in wind tunnel tests,” *Aerospace Engineering Journal*, vol. 54, no. 2, pp. 230–240, 2017.
- [6] NASA, “Testing on the ground before you fly: Wind tunnels at nasa ames,” 2022.
- [7] D. Way, P. Desai, W. Engelund, J. Cruz, and S. Hughes, *Design and Analysis of the Drop Test Vehicle for the Mars Exploration Rover Parachute Structural Tests*.
- [8] NASA, “Drop test,” 2025, accessed: 2025-01-26. [Online]. Available: <https://blogs.nasa.gov/commercialcrew/tag/drop-test/>

- [9] E. S. A. (ESA), “Supersonic parachute testing,” 2017, image. [Online]. Available: https://www.esa.int/ESA_Multimedia/Images/2017/07/Supersonic_parachute_testing
- [10] ——, “The atmospheric reentry demonstrator,” Directorate of Manned Spaceflight and Microgravity, Tech. Rep. BR-138, 1998, accessed: 2025-01-26. [Online]. Available: <https://www.esa.int/esapub/br/br138/br138.pdf>
- [11] J. A. E. A. (JAXA), “Orbital re-entry experiment (orex),” 2025, accessed: 2025-01-26. [Online]. Available: <https://global.jaxa.jp/projects/rockets/orex/index.html>
- [12] NASA, “SpaceX demo-1 splashdown recovery,” 2019, accessed: 2025-01-26. [Online]. Available: <https://www.nasa.gov/image-article/spacex-demo-1-splashdown-recovery-i/>
- [13] ——, “Top 10 things to know for NASA’s SpaceX Demo-2 return,” 2020, accessed: 2025-01-26. [Online]. Available: <https://www.nasa.gov/humans-in-space/top-10-things-to-know-for-nasas-spacex-demo-2-return/>
- [14] P. Bradshaw, *An Introduction to Turbulence and its Measurement*. Pergamon Press, 1971.
- [15] F. R. da Silva and S. R. de Oliveira, “Wind tunnel simulation of atmospheric boundary layer flows,” *Revista Engenharia Agrícola*, vol. 22, no. 3, pp. 249–257, 2002. [Online]. Available: <https://doi.org/10.1590/S0100-73862002000300005>

- [16] T. Ikeda and P. A. Durbin, “Direct simulations of a rough-wall channel flow,” *Journal of Fluid Mechanics*, vol. 571, p. 235–263, 2007.
- [17] R. M. Kawatani T, “Turbulence and wind speed characteristics within a model canopy flow field,” *fluid dynamics and diffusion laboratory, colorado state university, fort collins, colo (USA)*, 1969.
- [18] Y. A. Kosugi, M. Tateishi, “Improvement of the active turbulence generator and estimates of the turbulence field.”
- [19] H. Makita and K. Sassa, “Active turbulence generation in a laboratory wind tunnel,” *Dept. of Energy Eng., Toyohashi Univ. of Technology, 1-1 Tempaku-cho, Toyohashi 441, Japan*, 1991.
- [20] E. M. Lars Pepermans, “Comparison of various parachute deployment systems for full rocket recovery of sounding rockets,” *7 th European Conference For Aeronautics And Aerospace Sciences (EUCASS)*, 2017.
- [21] Spaceport Rocketry, “Dual-event recovery information,” accessed: 2024-07-07.
- [22] V. I. M. S. V. Leonov and A. T. Ponomarev, “Shape modeling and strength analysis of parachutes,” *Prof. Zhukovskii and Gagarin Air Force Engineering Academy*, 2010.
- [23] D. S. Pascual, “Recovery system design for lower stages of rockets,” 2017, bachelor’s thesis, UNIVERSITY OF RWTH AACHEN, 2017.

- [24] I. J. Thomas Britting, “Design, manufacture, and validation of a student-made ringsail parachute for sounding rocket recovery,” *4 th Symposium on Space Educational Activities*, 2022.
- [25] E. Berger, *Structural Analysis and Design of Wind Tunnel Test Rigs*, 2009.
- [26] D. Smith and K. Jones, “Minimizing aerodynamic interference in test rig design,” *AIAA Journal*, vol. 50, no. 9, pp. 1849–1857, 2012.
- [27] M. Huang, W. Wang, and J. Li, “Analysis and verification of aerodynamic characteristics of tianwen-1 mars parachute,” *Space: Science & Technology*, vol. 2022, 2022. [Online]. Available: <https://spj.science.org/doi/abs/10.34133/2022/9805457>
- [28] J. M. Macha, “An introduction to testing parachutes in wind tunnels,” *AIAA Journal*, no. 6101577. [Online]. Available: <https://www.osti.gov/biblio/6101577>
- [29] G. R. centre. (2023) Shape effects on drag coefficient. [Online]. Available:

6 Appendix

A Time Plan

Table A.1: Budget

B Budget

Table B.1: Budget

ITEM	DESCRIPTION	Price(Ksh)	Quantity	TOTAL COST(Ksh)
Micro-controller	Arduino Mega 2560	2200	1	2200
Force Sensors	Load cell, 20kgf	400	1	400
Flexible Couplers	8mm Diameter	300	5	1500
Power Supply	12V PSU	1500	1	1500
Stepper Motors	Nema 17	2500	5	12500
Motor drivers	DRV 8825	200	5	1000
Buck converter	DC-DC buck	300	1	300
Parachutes	Drogue	1000	1	1000
	Main	1000	1	1000
	Model	200	2	400
Ball bearings	Sealed	200	5	1000
Acrylic	Adhesive	200	5	1000
Test rig	Rod and Support	640	1	640
TOTAL	-			24, 440

C Drawings

C.1 Active grid system design drawing

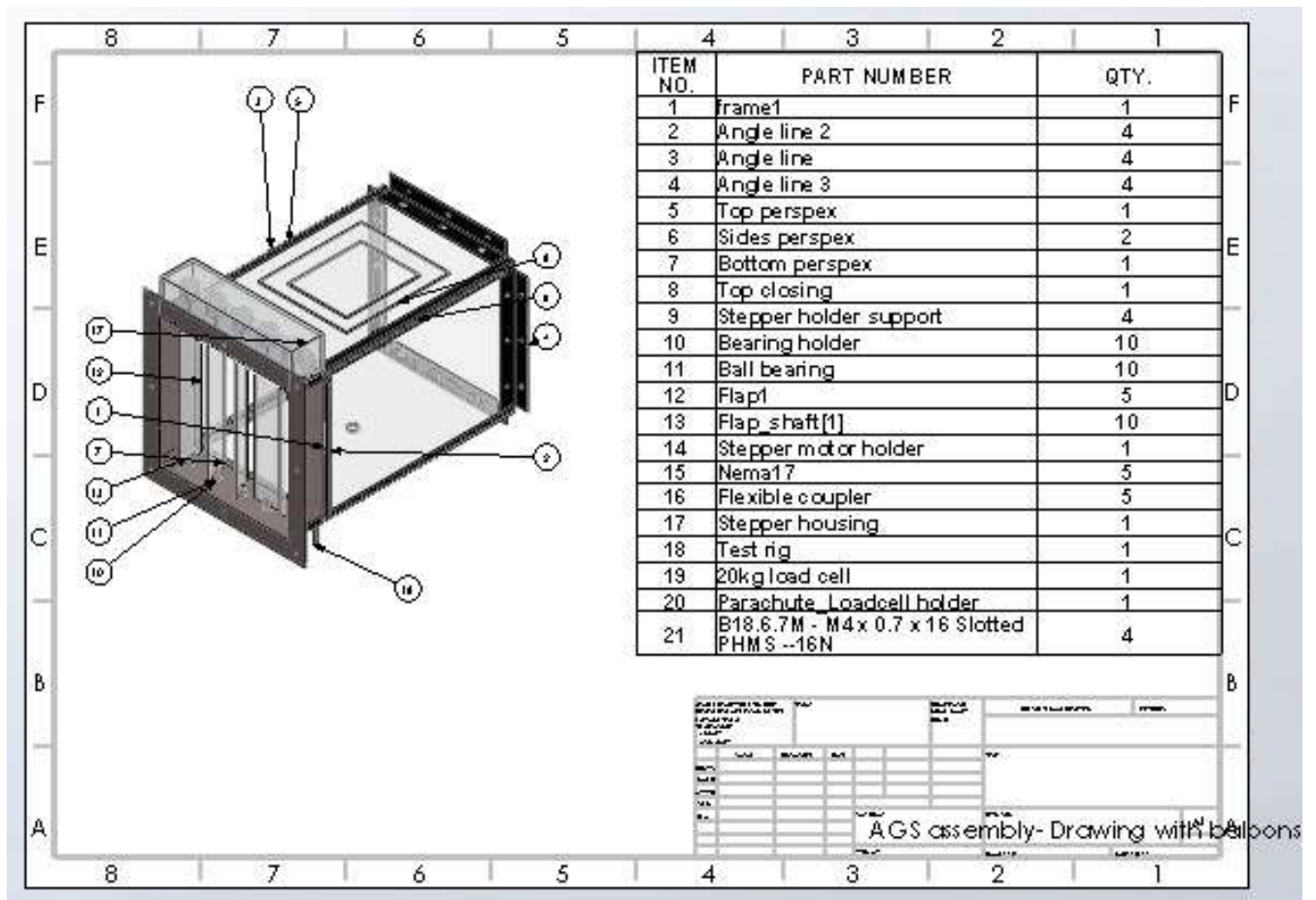


Figure C.1: Active grid system design drawing

C.2 Parachute holder drawing

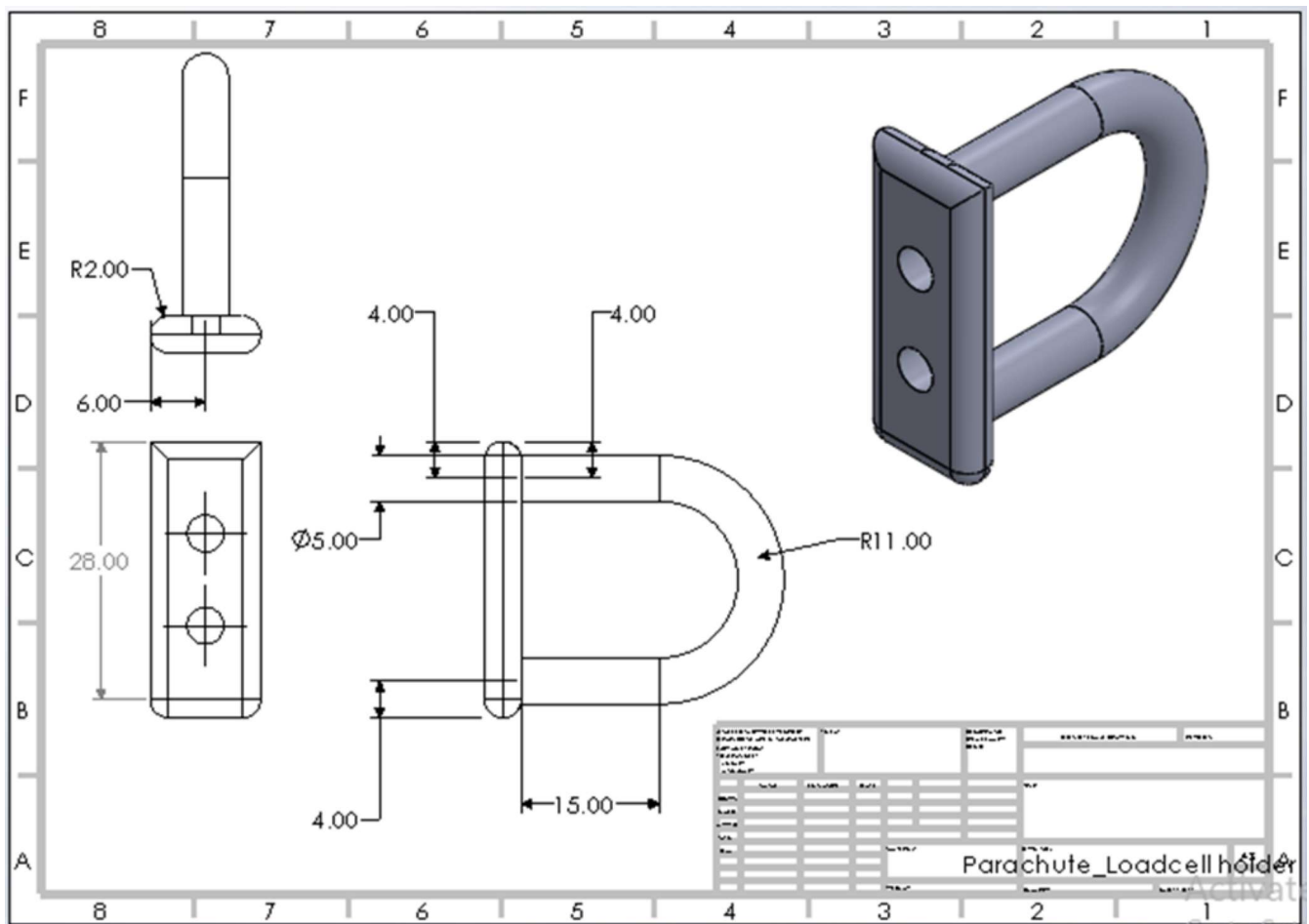


Figure C.2: Parachute holder design drawing

C.3 Test rig design drawing

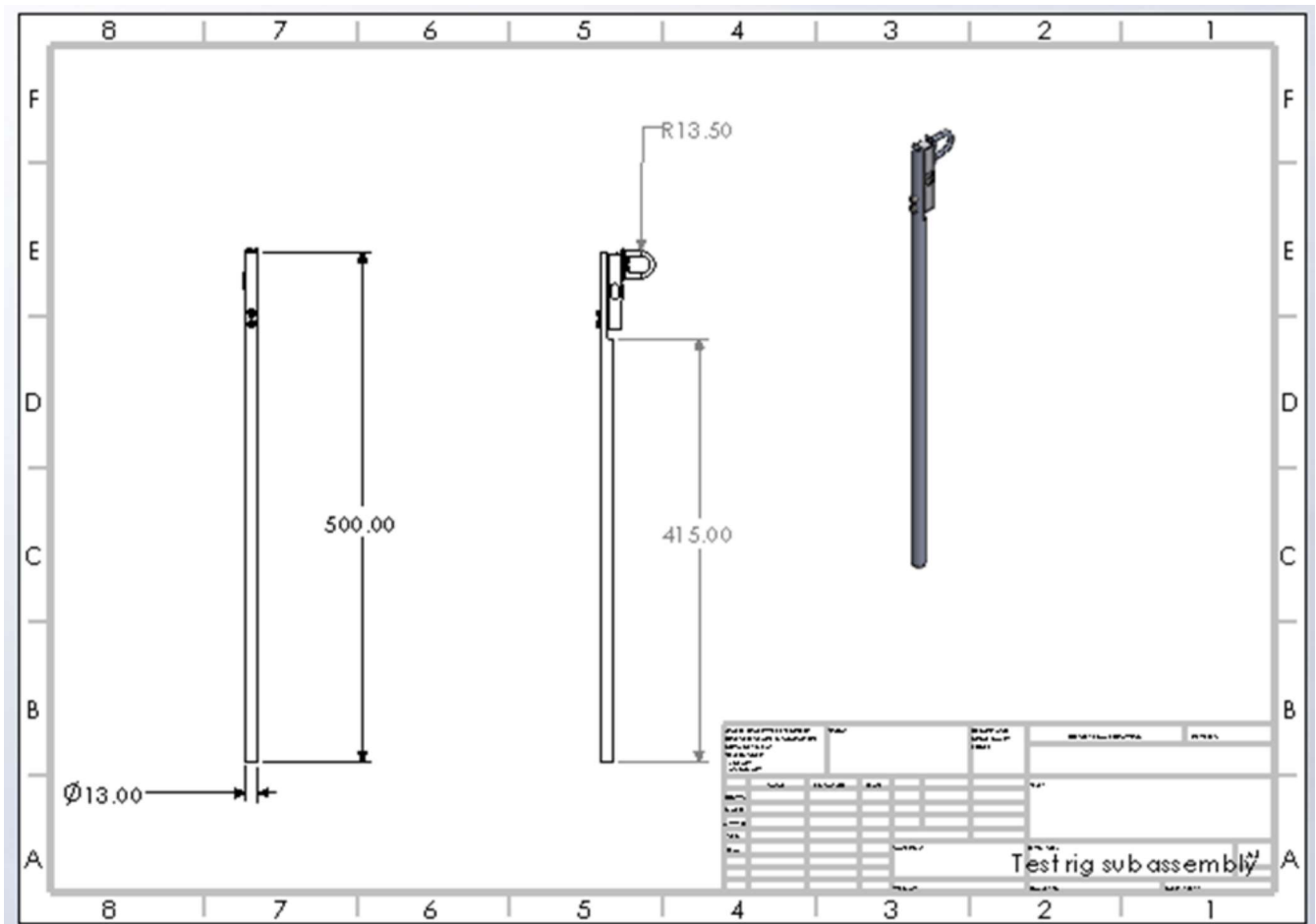


Figure C.3: Test rig design drawing

C.4 Frame design drawing

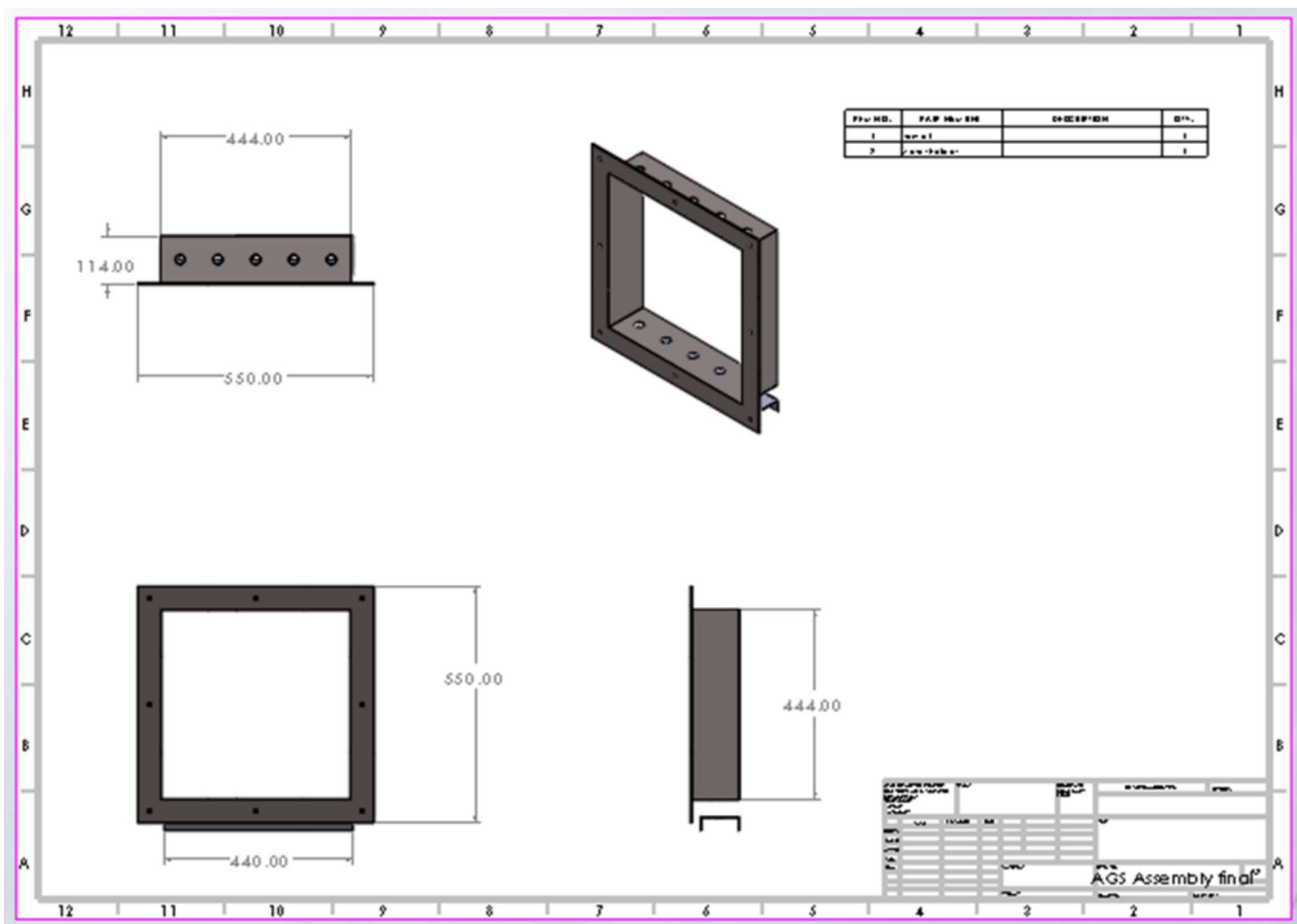


Figure C.4: Frame design drawing

C.5 Flap shaft design drawing

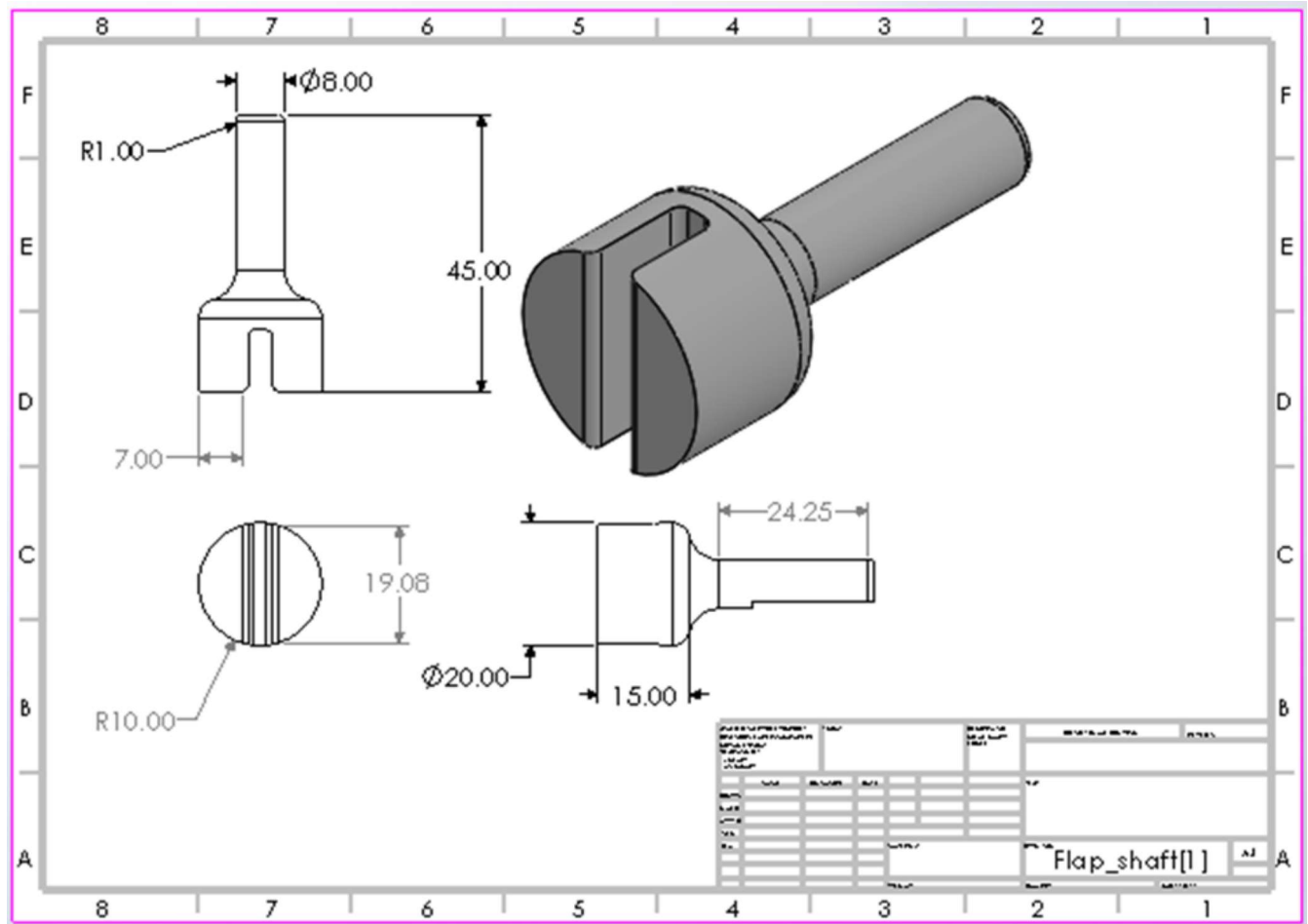


Figure C.5: Flap shaft design drawing

C.6 Flap design drawing

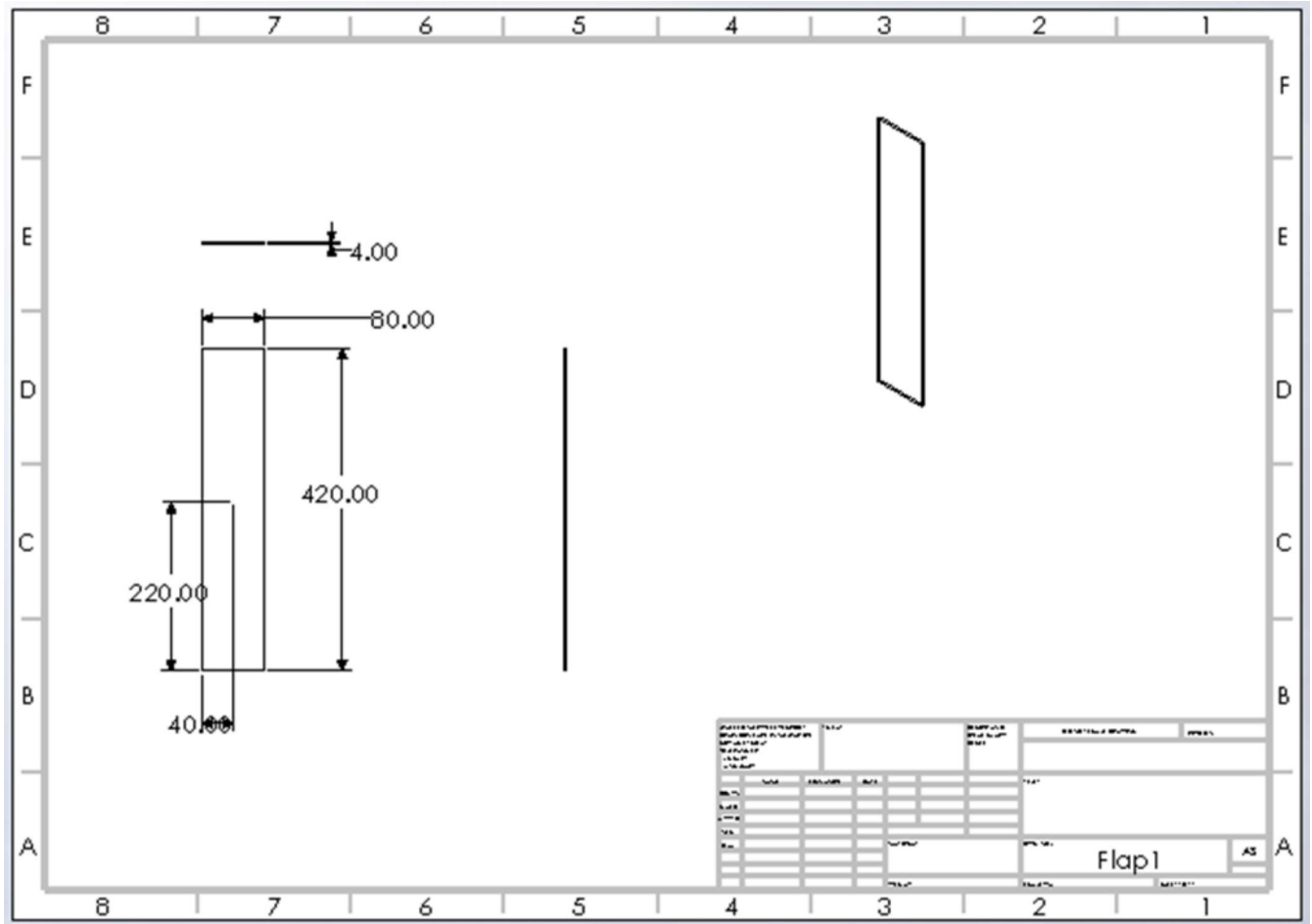


Figure C.6: Flap design drawing

C.7 Limit switch subassembly design drawing

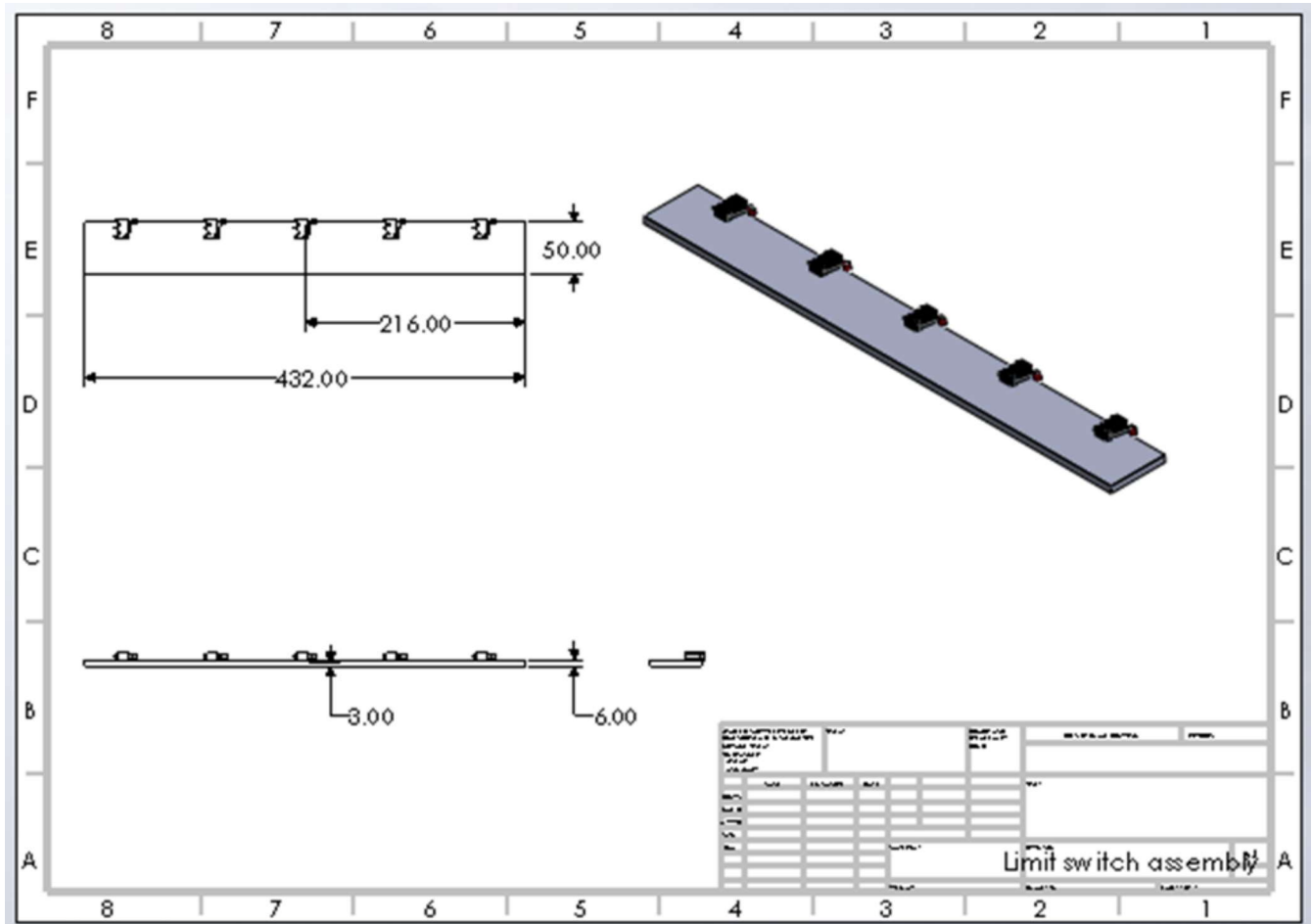


Figure C.7: Limit switch drawing

C.8 Top perspex design drawing

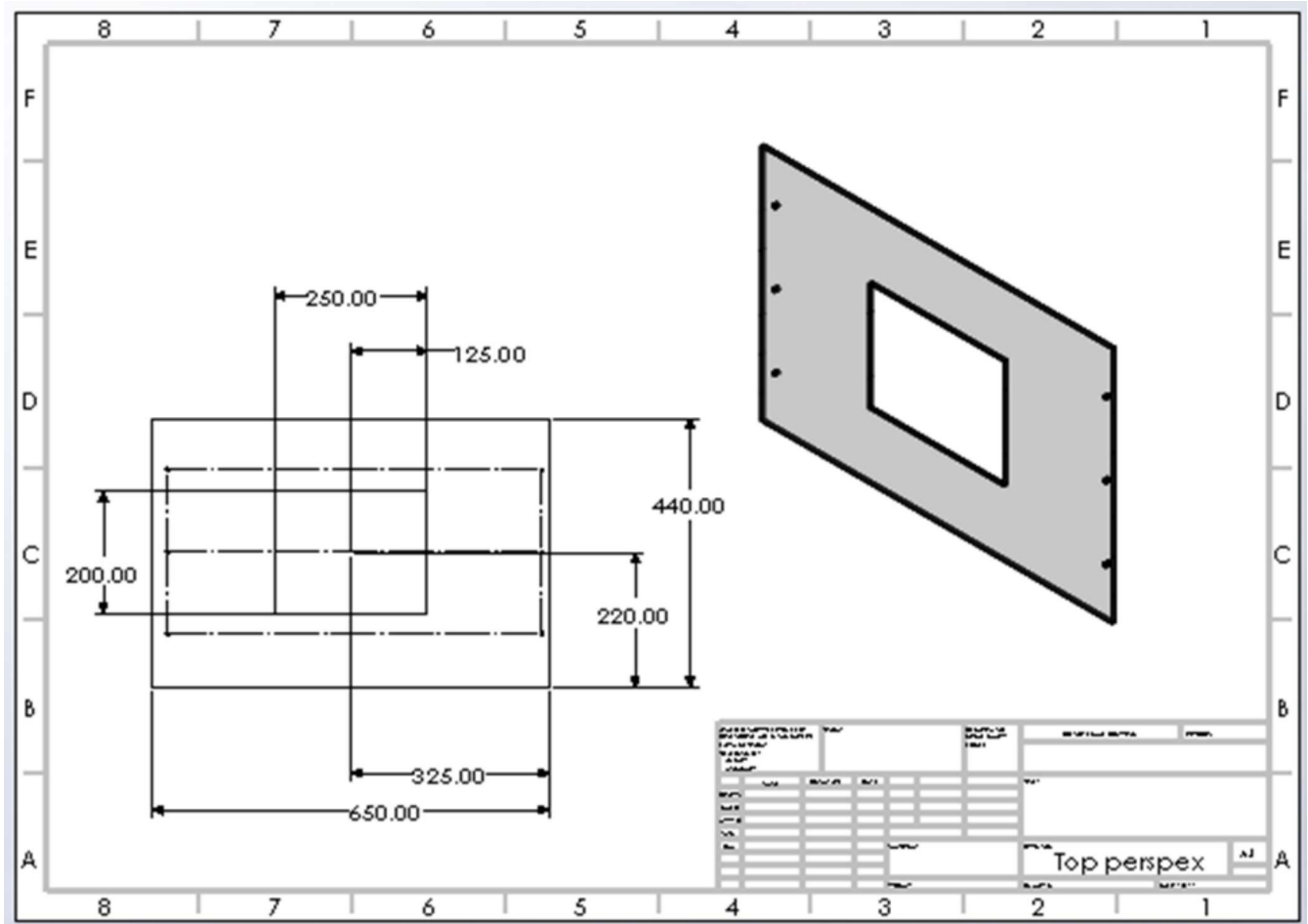


Figure C.8: Top perspex design drawing

C.9 Bottom perspex design drawing

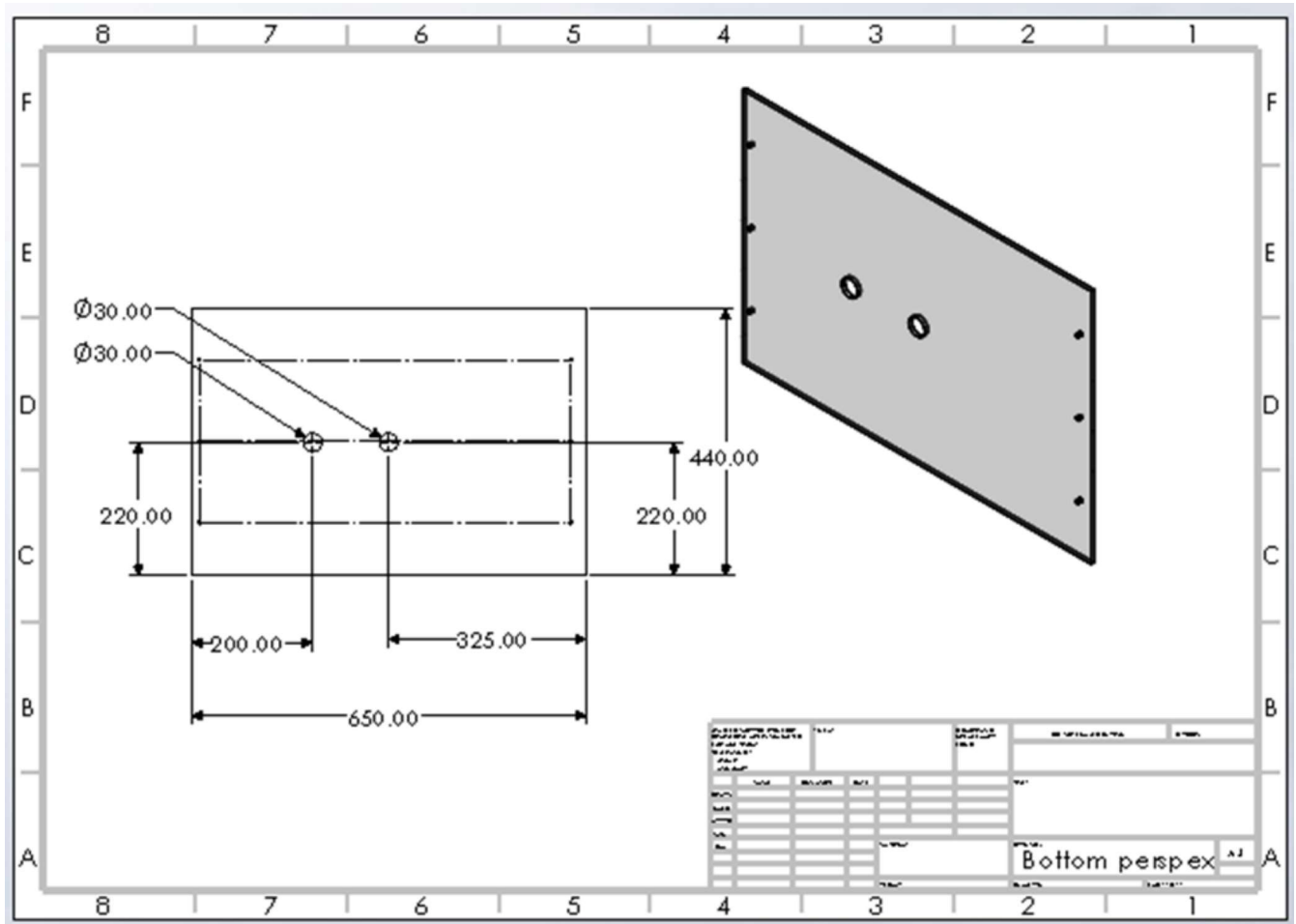


Figure C.9: Bottom perspex design drawing

C.10 Sides perspex design drawing

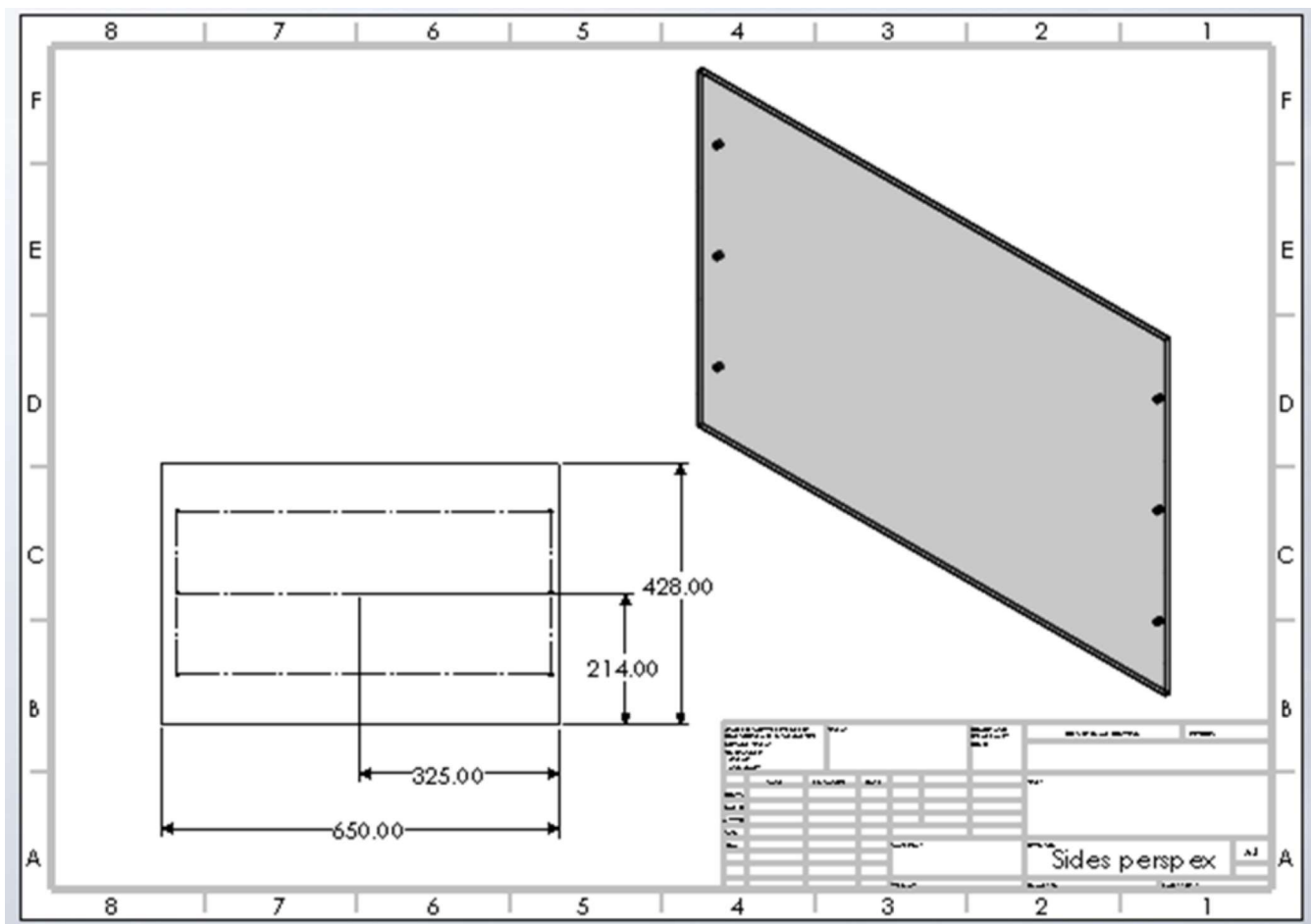


Figure C.10: Side perspex design drawing

C.11 Circuit board housing design drawing

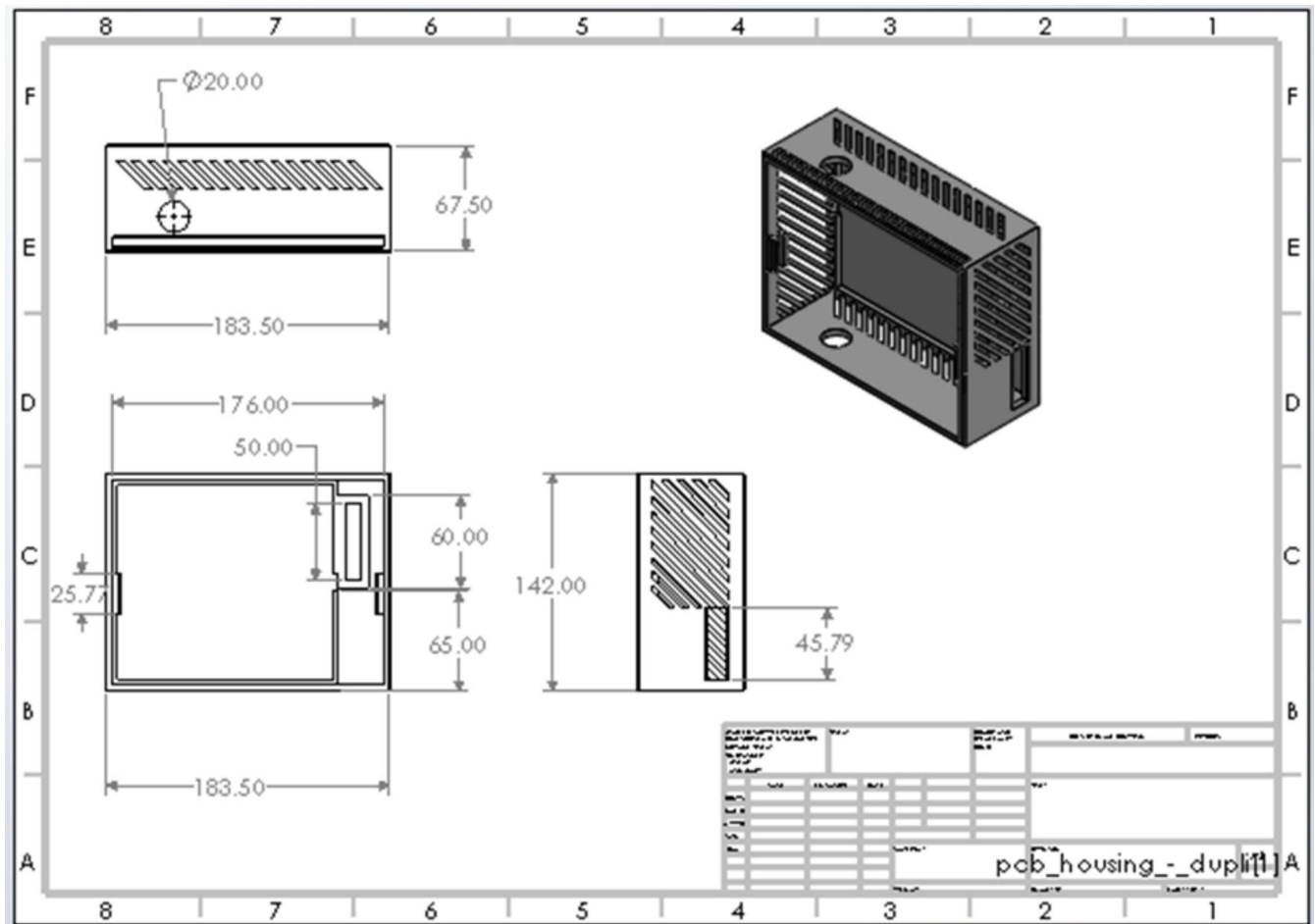


Figure C.11: Bottom perspex design drawing